

# L2SR: Learning to Sample and Reconstruct for Accelerated MRI

Pu Yang

School of Mathematical Sciences, Peking University  
yang\_pu@pku.edu.cn

Bin Dong

Beijing International Center for Mathematical Research, Peking University  
dongbin@math.pku.edu.cn

## Abstract

*Accelerated MRI aims to find a pair of samplers and reconstructors to reduce acquisition time while maintaining the reconstruction quality. Most of the existing works focus on finding either sparse samplers with a fixed reconstructor or finding reconstructors with a fixed sampler. Recently, people have begun to consider learning samplers and reconstructors jointly. In this paper, we propose an alternating training framework for finding a good pair of samplers and reconstructors via deep reinforcement learning (RL). In particular, we propose a novel sparse-reward Partially Observed Markov Decision Process (POMDP) to formulate the MRI sampling trajectory. Compared to the existing works that utilize dense-reward POMDPs, the proposed sparse-reward POMDP is more computationally efficient and has a provable advantage over dense-reward POMDPs. We evaluate our method on fastMRI, a public benchmark MRI dataset, and it achieves state-of-the-art reconstruction performances.*

## 1. Introduction

Magnetic resonance imaging (MRI) is widely used in clinical studies without the risk of radiation exposure. However, MRI has the inherent disadvantage of a slow data acquisition process, which limits its wider clinical use.

Compressed sensing (CS) [4] techniques are introduced in MRI to reduce the number of sampling, thereby speeding up the MRI scanning process. Traditional CS-MRI [16, 17] first subsamples measurements in the Fourier domain with heuristic sampling policies such as random sampling according to a given heuristic distribution and then reconstructs MR images by solving an ill-posed reconstruction inverse problem. These optimization-based methods are interpretable and with theoretical guarantees. Although it has

notably reduced acquisition time compared to commercial MRI, there is still tremendous room for improvement. Recently, deep learning (DL) models [9, 11, 14, 20, 33, 34, 37] have been used as reconstructors for MRI, which significantly improve reconstruction quality. These models utilize heuristic sampling policies similar to CS-MRI and learn reconstructors from a specific dataset.

One way to quantify the quality of sampling policies and reconstructors is by examining its acceleration-quality trade-off. The heuristic sampling policies may have a limited acceleration-quality trade-off, as they cannot adaptively decide the sampling strategy according to the anatomical structures of patients. To learn an adaptive sampling policy rather than by human design, one of the approaches [12] utilizes Monte Carlo Tree Search (MCTS) to learn a progressive sampler by self-supervised training. Another approach formulates the sampling trajectory as a Markov Decision Process (MDP) and solves it via deep Reinforcement Learning (RL). Such dynamic sampling method was first proposed in Computed Tomography (CT) scanning by [25] and a similar idea was later proposed in the MRI region. More recently, [2, 15, 19] propose to learn parametric samplers with a fixed pre-trained reconstructor via deep RL.

Since finding either reconstructors with a fixed heuristic sampling policy or sparse samplers with a fixed reconstructor may result in a suboptimal solution, [1, 12, 27, 35] aim to improve the sampling speed and the reconstruction quality by finding a good pair of sampler and reconstructor.

In this paper, we propose an alternating training framework for finding a good pair of samplers and reconstructors via deep reinforcement learning (RL). We refer to this framework as L2SR, which is short for Learning to Sample and Reconstruct. In particular, we formulate the MRI sampling trajectory as a novel sparse-reward Partially Observed Markov Decision Process (POMDP). Compared to [2, 15, 19] that use dense-reward POMDPs, the proposed

sparse-reward POMDP does reconstruction only at the terminal state rather than every intermediate state. Therefore, it is more computationally efficient and has a provable advantage over dense-reward POMDPs. In addition, the proposed sparse-reward POMDP derives a new joint optimization problem that allows alternating training of samplers and reconstructors. We compare the proposed L2SR to current state-of-the-art methods on fastMRI dataset [36] under various settings, and it achieves the best reconstruction performance for fixed acceleration factors.

The remainder of this paper is organized as follows. In Sec. 2, we discuss related works. In Sec. 3, we provide notations of accelerated MRI and formulate optimization problems. In Sec. 4, We analyze the design flaws of the dense-reward POMDP. In Sec. 5, we propose the sparse-reward POMDP and the alternating training framework. In Sec. 6, we show experimental results. In Sec. 7, we make a conclusion.

## 2. Related Work

In this section, we briefly review prior works on sampling and reconstruction in accelerated MRI.

### 2.1. Learning Reconstructors with Heuristic Sampling

Existing heuristic sampling policies [6, 16, 29] include uniform density random sampling, variable density sampling, Poisson-disc sampling, equispaced sampling, and continuous-trajectory variable density sampling. These sampling strategies are very simple and easy to implement. Methods of learning reconstructors with a fixed heuristic sampling policy can be divided into two categories: optimization-based methods and DL-based methods.

**Optimization-based methods** obtain the reconstruction image by solving constrained optimization problems which minimize a  $\ell_1$ -norm regularization term for sparsity and constrains the  $\ell_2$ -norm error in  $k$ -space for accuracy (see Eq.[3] in [16]). The regularization term is often referred to as Total Variation (TV) [23] or Wavelet [5]. The optimization problems can be solved by hand-crafted priors along with iterative optimization methods, such as Iterative Soft Thresholding Algorithm (ISTA) [7] and Iterative Reweighted Least Squares (IRLS) [8]. These methods are interpretable and with theoretical guarantees. However, the optimization problems depend on image priors by human design, thereby are not adaptive to specific datasets.

**DL-based methods** use DL models as reconstructors for MRI, which significantly improves reconstruction quality. Unet-based network models [11, 14] and GAN-based network models [20, 33] learn an end-to-end mapping from sampled measurements to reconstruction images. Unrolled dynamic models such as ADMM-net [34], Variational-net [9], and ISTA-net [37] are designed by first unrolling an

iterative algorithm to form the backbone network architecture and then replacing some of its operators by neural networks. These methods are often data-driven, thus adaptive to a specific dataset. However, compared to optimization-based methods, DL-based methods are relatively less interpretable and may have generalization issues.

### 2.2. Learning Dynamic Sampling with Fixed Reconstructors via Deep RL

The heuristic sampling policies may have a limited acceleration-quality trade-off due to their lack of adaptivity to specific datasets. Since the sampling process is carried out over time, it can be viewed as a finite sequential decision-making process. Dynamic sampling methods [2, 15, 19] formulate the MRI sampling trajectory as a Partially Observed Markov Decision Process (POMDP) (see Sec. 3.2) and learn parametric samplers with a fixed pre-trained reconstructor by modern deep RL algorithms, such as DDQN [28] and policy gradient [3]. RL enables learning a non-greedy sequential decision function without relying on human heuristics. These methods use the RL-learned policies to guide the scanning based on the measurements collected in the preceding stage, thus achieving a data-adaptive and personalized scanning.

### 2.3. Jointly Learning Samplers and Reconstructors via Back-Propagation

If we fix a sampler to find an optimal reconstructor or fix a reconstructor to find an optimal sampler, we often obtain suboptimal pairs of samplers and reconstructors. Therefore, some recent works aim to learn a good pair of samplers and reconstructor for a better acceleration-quality trade-off. These works propose to jointly train samplers and reconstructors end-to-end by Back-Propagation (BP).

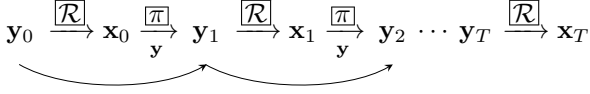
One line of works [1, 26, 30, 32, 38] use a learnable column vector of probabilistic sub-sampling masks  $\mathbf{p}$  as the sampler which is independent of the specific image and jointly train it together with a neural network based reconstruction model  $\mathcal{R}$ . These works learn a better sampler  $\mathbf{p}$  than human-designed heuristic sampling policies. However, these samplers are not adaptive to each specific image. The ideas of these works can be illustrated by the following diagram

$$\boxed{\mathbf{p}} \xrightarrow[\mathbf{y}]{\text{sample}} \mathbf{y}_T \xrightarrow{\boxed{\mathcal{R}}} \mathbf{x}_T$$

where the modules in the boxes are learnable.

Another line of works [12, 27, 35, 39] use a neural network based model  $\pi$  as the sampler which is adaptive to sampled measurements. The sampler  $\pi$  is jointly trained with a DL-based reconstructor  $\mathcal{R}$  end-to-end via BP. These methods learn sampling strategies that are adaptive to each image. However, the training of the sampler and the reconstructor by BP can be challenging. On one hand, gradients

are passed through long trajectories leading to gradient vanishing or exploding. On the other hand, GPU memory limits the size of neural networks due to long trajectories. Therefore, these works always turn to solve weakened forms of the joint optimization problem Eq. (1). The ideas of these works can be illustrated by the following diagram



where the modules in the boxes are learnable.

In this paper, we also aim to learn a pair of samplers and reconstructors jointly. Instead of training end-to-end by BP, we will design an RL-based joint training framework.

### 3. Problem Formulation

In Sec. 3.1, we specify the notation of CSMRI. In Sec. 3.2, we formulate the optimization problem.

#### 3.1. Notation

In this paper, we only consider 2D accelerated MRI and 1D vertical Cartesian sampling. Let  $\mathbf{x} \in \mathbb{R}^{N \times N}$  be a ground truth image, and  $\mathbf{y} \in \mathbb{C}^{N \times N}$  be the fully sampled measurements in Fourier domain (also called k-space) via 2D Discrete Fourier Transform  $\mathcal{F}$ , i.e.,  $\mathbf{y} = \mathcal{F}(\mathbf{x})$ . We denote  $\mathcal{D}$  as a dataset containing ground truth images. Accelerated MRI acquires measurements in the Fourier domain by masking  $\mathbf{y}$  with a binary mask matrix  $\mathbf{M} \in \{0, 1\}^{N \times N}$ , that is, we can only observe  $\mathbf{M} \odot \mathbf{y}$  where  $\odot$  denotes multiplying the corresponding terms of two matrices. A reconstructor is a mapping  $\mathcal{R} : \mathbb{C}^{N \times N} \rightarrow \mathbb{R}^{N \times N}$ , which is usually a parametric neural network denoted as  $\mathcal{R}(\cdot; \theta_{\mathcal{R}})$ . A heuristic sampling policy  $\pi_t^h$  is a probability distributional function taking the binary column vector  $\mathbf{a}$  as input.  $\pi_t^h$  samples  $\mathbf{a}$  satisfying  $\|\mathbf{a}\|_1 = t$  which derives a mask matrix  $\mathbf{M}^{\mathbf{a}} = \mathbf{1} \cdot \mathbf{a}^T$  satisfying  $\|\mathbf{M}^{\mathbf{a}}\|_{\infty} = \|\mathbf{a}\|_1$ .

We give a list of notation index and where it is defined in Appendix A.

#### 3.2. Optimization Problems

To get an optimal pair of samplers and reconstructors, we want to solve the following joint optimization problem based on dense-reward POMDP

$$\begin{aligned} & \max_{\theta_{\pi}, \theta_{\mathcal{R}}} \mathbb{E}_{\mathbf{x} \sim \mathcal{D}} \mathbb{E}_{\pi} \ell(\mathbf{x}_T, \mathbf{x}) \\ \text{s.t. } & \mathbf{y}_t = \mathbf{M}_t \odot \mathcal{F}(\mathbf{x}), \quad t = 0, 1, \dots, T \\ & \mathbf{x}_t = \mathcal{R}(\mathbf{y}_t; \theta_{\mathcal{R}}), \quad t = 0, 1, \dots, T \\ & a_t \sim \pi(\cdot | \mathbf{x}_t; \theta_{\pi}), \quad t = 0, 1, \dots, T-1 \\ & \mathbf{M}_{t+1} = \mathbf{M}_t + \mathbf{M}^{a_t}, \quad t = 0, 1, \dots, T-1 \end{aligned} \quad (1)$$

where  $a_t \in \mathcal{A} = \{n\}_{n=1}^N$  and the sampler  $\pi : \mathcal{A} \times \mathbb{R}^{N \times N} \rightarrow [0, 1]$  is a discrete conditional probability distribution function.

For simplicity, we write it in an unconstrained form:

$$\max_{\theta_{\pi}, \theta_{\mathcal{R}}} \mathbb{E}_{\mathbf{x} \sim \mathcal{D}} J_T^{\text{dense}}(\mathbf{x}; \pi, \mathcal{R}) \quad (2)$$

There is a huge challenge to solve this joint optimization problem directly. One of the approaches is to jointly train  $\theta_{\pi}$  and  $\theta_{\mathcal{R}}$  end-to-end by BP as mentioned in Sec. 2.3. However, as the training may fail due to the long sampling trajectory, existing BP methods always turn to solve weakened forms of Eq. (1). Another approach is to use RL. The existing dense-reward POMDP may not be suitable for end-to-end joint training, since we should keep the environment unchanged when training the sampler via RL, thereby the reconstructor as a part of the environment also should remain the same, which contradicts the end-to-end joint training. In addition, it is hard to design a multi-agent POMDP for the two learnable agents, the sampler  $\pi$  and the reconstructor  $\mathcal{R}$ .

DL-based MRI methods get a better reconstructor with a fixed heuristic sampling policy  $\pi^h$  by solving the following suboptimization problem of Eq. (2)

$$\max_{\theta_{\mathcal{R}}} \mathbb{E}_{\mathbf{x} \sim \mathcal{D}} \mathbb{E}_{\mathbf{a} \sim \pi^h} [\ell(\mathcal{R}(\mathbf{M}^{\mathbf{a}} \odot \mathcal{F}(\mathbf{x})), \mathbf{x})] \quad (3)$$

Dynamic sampling methods obtain better samplers by solving the following suboptimization problem of Eq. (2) with a fixed pre-trained reconstruction model  $\mathcal{R}(\cdot)$

$$\max_{\theta_{\pi}} \mathbb{E}_{\mathbf{x} \sim \mathcal{D}} J_T^{\text{dense}}(\mathbf{x}; \pi, \mathcal{R}) \quad (4)$$

To solve Eq. (4), they formulate the sequential sampling process as the following *dense-reward POMDP*:

- Observation

$$\mathbf{y}_t = \mathbf{M}_t \odot \mathbf{y}, \quad t = 0, 1, \dots, T \quad (5)$$

$$\mathbf{x}_t = \mathcal{R}(\mathbf{y}_t), \quad t = 0, 1, \dots, T \quad (6)$$

where  $\mathbf{M}_0$  is an initial binary mask matrix.

- Action set  $\mathcal{A}$  and action  $a_t \in \mathcal{A}$

$$a_t \sim \pi(\cdot | \mathbf{x}_t), \quad t = 0, 1, \dots, T-1 \quad (7)$$

- Transition

$$\mathbf{M}_{t+1} = \mathbf{M}_t + \mathbf{M}^{a_t}, \quad t = 0, 1, \dots, T-1 \quad (8)$$

and  $\mathbf{y}_{t+1}$  and  $\mathbf{x}_{t+1}$  is calculated by Eq. (5) and Eq. (6).

- Reward

$$r_t = \ell(\mathbf{x}_t, \mathbf{x}) - \ell(\mathbf{x}_{t-1}, \mathbf{x}), \quad t = 1, \dots, T \quad (9)$$

where  $\ell$  is an image similarity metric. In this paper, we always use structural similarity index measure (SSIM) [31] as the similarity metric.

- Discount factor  $\gamma \in [0, 1]$

These methods solve Eq. (4) via deep RL with the above dense-reward POMDP.

However, [35] have revealed the *training mismatch* of solving this suboptimization problem (Eq. (4)), that is, the heuristic sampling policy used to pre-train the reconstructor is different from the RL-learned policy. The training mismatch leads to a suboptimal pair of samplers and reconstructors of the joint optimization problem (Eq. (2)).

## 4. The Issues with Dense-reward POMDP

Besides the training mismatch problem caused by solving the suboptimization problem, we further analyze the dense-reward POMDP and identify problems caused by the MDP design. The dense-reward POMDP incorporates reconstructions into the environment, specifically into transitions and rewards, that leads to two issues: *high computational cost* and *distributional mismatch*. They are the motivation for us to propose the sparse-reward POMDP in the next section.

### 4.1. High Computational Cost

Since reconstructions are involved in the transition, the dense-reward POMDP first does reconstruction (Eq. (6)) and then does sampling (Eq. (7)) at each step in the inference process. It is very time-consuming to do so many reconstructions. However, the dynamic sampling method for CT scanning [25] uses original sampling signals rather than reconstruction images as the input of the sampler, which is more computationally efficient. We will find a better POMDP that does only one reconstruction in the inference process.

### 4.2. Distributional Mismatch

Since reconstructions are involved in the rewards (Eq. (9)), the dense-reward POMDP requires evaluating the similarity of the ground truth and the reconstruction image  $\ell(\mathbf{x}_t, \mathbf{x})$  in every intermediate state. Therefore, the dense-reward POMDP requires a reliable reconstructor for all the intermediate states, which means the reconstructor should be pre-trained with a mixture of heuristic sampling policy  $\pi_{\text{mix}}^h = \sum_{t=\|\mathbf{M}_0\|_\infty}^{\|\mathbf{M}_0\|_\infty+T} c_t \pi_t^h$  where  $\sum c_t = 1$ , instead of only the terminal sampling policy  $\pi_{T+\|\mathbf{M}_0\|_\infty}^h$ . However, as we

will show later, this may not help with the final reconstruction performance, i.e., the optimal value of the joint optimization problem (Eq. (2)). We will justify this claim in Theorem 2.

## 5. The Proposed Method

### 5.1. Sparse-Reward POMDP

To improve inference efficiency and eliminate the distributional mismatch, we reconstruct after finishing sampling the entire trajectory and get a non-zero reward after the final reconstruction. Specifically, we propose the following *sparse-reward POMDP*:

- Observation

$$\mathbf{y}_t = \mathbf{M}_t \odot \mathbf{y}, \quad t = 0, 1, \dots, T \quad (10)$$

where  $\mathbf{M}_0$  is an initial binary mask matrix.

- Action set  $\mathcal{A}$  and action  $a_t \in \mathcal{A}$

$$a_t \sim \pi(\cdot | \mathbf{y}_t), \quad t = 0, 1, \dots, T-1 \quad (11)$$

where the sampler  $\pi : \mathcal{A} \times \mathbb{C}^{N \times N} \rightarrow [0, 1]$  is a discrete conditional probability distribution function.

- Transition

$$\mathbf{M}_{t+1} = \mathbf{M}_t + \mathbf{M}^{a_t}, \quad t = 0, 1, \dots, T-1 \quad (12)$$

and  $\mathbf{y}_t$  is calculated by Eq. (10)

- Reward

$$\begin{cases} r_t = 0, & t = 1, \dots, T-1 \\ r_T = \ell(\mathcal{R}(\mathbf{y}_T), \mathbf{x}) \end{cases} \quad (13)$$

- Discount factor

$$\gamma = 1 \quad (14)$$

It derives a sparse-reward joint optimization problem:

$$\begin{aligned} & \max_{\theta_\pi, \theta_{\mathcal{R}}} \mathbb{E}_{\mathbf{x} \sim \mathcal{D}} \mathbb{E}_\pi \ell(\mathcal{R}(\mathbf{y}_T), \mathbf{x}) \\ & \text{s.t. } \mathbf{y}_t = \mathbf{M}_t \odot \mathcal{F}(\mathbf{x}), \quad t = 0, 1, \dots, T \\ & \quad a_t \sim \pi(\cdot | \mathbf{y}_t; \theta_\pi), \quad t = 0, 1, \dots, T-1 \\ & \quad \mathbf{M}_{t+1} = \mathbf{M}_t + \mathbf{M}^{a_t}, \quad t = 0, 1, \dots, T-1 \end{aligned} \quad (15)$$

and its unconstrained form:

$$\max_{\theta_\pi, \theta_{\mathcal{R}}} \mathbb{E}_{\mathbf{x} \sim \mathcal{D}} J_T^{\text{sparse}}(\mathbf{x}) \quad (16)$$

Solving the sparse-reward joint optimization problem will yield a reconstructor and a sampler that is no weaker than the dense-reward joint optimization problem. We formulate this claim as the following theorem.

**Theorem 1 (joint optimization problem)** For a sufficiently wide (or deep) fully connected neural network set  $\mathcal{H}$ , if a discrete distribution  $\pi : \mathbb{R}^{n \times n} \rightarrow \mathbb{R}^n$  and a reconstructor  $\mathcal{R} : \mathbb{C}^{n \times n} \rightarrow \mathbb{R}^{n \times n}$  is continuous, a similarity metric  $\ell : [\mathbb{R}^{n \times n}, \mathbb{R}^{n \times n}] \rightarrow \mathbb{R}[0, 1]$  is  $\delta$ -Lip, then the optimal values of optimization problems Eq. (1) and Eq. (15) satisfy

$$\max_{\pi, \mathcal{R} \in \mathcal{H}} \mathbb{E}_{\mathbf{x} \sim \mathcal{D}} J_T^{\text{dense}}(\mathbf{x}) \leq \max_{\pi, \mathcal{R} \in \mathcal{H}} \mathbb{E}_{\mathbf{x} \sim \mathcal{D}} J_T^{\text{sparse}}(\mathbf{x}) \quad (17)$$

We leave the proof in Appendix B.1.

This theorem guarantees that we can switch to solve the sparse-reward joint optimization (Eq. (15)) instead of the dense-reward one (Eq. (1)).

Next, we will show that sparse-reward POMDP is more computationally efficient. The inference process of the dense-reward POMDP is

$$y_0 \xrightarrow{\mathcal{R}} x_0 \xrightarrow{\pi} y_1 \xrightarrow{\mathcal{R}} x_1 \xrightarrow{\pi} y_2 \cdots y_T \xrightarrow{\mathcal{R}} x_T$$

and that of the proposed sparse-reward POMDP is

$$y_0 \xrightarrow{\pi} y_1 \xrightarrow{\pi} y_2 \cdots y_T \xrightarrow{\mathcal{R}} x_T$$

One can see that the sparse-reward POMDP does not need to do reconstruction at the sampling stage, which saves  $T$  times of reconstruction compared to dense-reward POMDP in each inference process, thus saving time.

Then, we will theoretically explain how sparse-reward POMDP avoids the distributional mismatch in dense-reward POMDP. Since the reconstructor only works on the terminal state to get the reward, we use a terminal heuristic sampling policy  $\pi_T^h$  for pre-training the reconstructor  $\mathcal{R}(\cdot)$ . We can learn samplers with the proposed sparse-reward POMDP by solving the following suboptimization problem of Eq. (16) with a fixed pre-trained reconstruction model

$$\max_{\theta_\pi} \mathbb{E}_{\mathbf{x} \sim \mathcal{D}} J_T^{\text{sparse}}(\mathbf{x}; \mathcal{R}) \quad (18)$$

The following theorem guarantees that the sparse-reward suboptimization problem (Eq. (18)) yields a sampler no weaker than the dense-reward one (Eq. (4)), which formulates the claim in the above section.

**Theorem 2 (distributional mismatch)** With the same assumptions in Theorem 1, let  $T_+ = T + \|\mathbf{M}_0\|_\infty$  and given a terminal sampling policy  $\pi_{T_+}^h$  satisfying that  $\forall \mathbf{a}, \|\mathbf{a}\|_1 =$

$T_+$  satisfies  $\pi_{T_+}^h(\mathbf{a}) > 0$ . If there is a reconstructor  $\mathcal{R}^{\text{sparse}}$  satisfying

$$\mathcal{R}^{\text{sparse}} \in \operatorname{argmax}_{\mathcal{R} \in C} \mathbb{E}_{\mathbf{x} \sim \mathcal{D}} \mathbb{E}_{\mathbf{a} \sim \pi_{T_+}^h} \ell(\mathcal{R}(\mathbf{M}^{\mathbf{a}} \odot \mathcal{F}(\mathbf{x})), \mathbf{x}) \quad (19)$$

then, for any reconstructor  $\mathcal{R}^{\text{dense}} \in C$ , we have

$$\max_{\pi \in \mathcal{H}} \mathbb{E}_{\mathbf{x} \sim \mathcal{D}} J_T^{\text{dense}}(\mathbf{x}; \mathcal{R}^{\text{dense}}) \leq \max_{\pi \in \mathcal{H}} \mathbb{E}_{\mathbf{x} \sim \mathcal{D}} J_T^{\text{sparse}}(\mathbf{x}; \mathcal{R}^{\text{sparse}}) \quad (20)$$

We leave the proof in Appendix B.2.

**Remark 1.** This theorem demonstrates that the optimal value of Eq. (4) is no greater than that of Eq. (18). Therefore, in terms of pre-training  $\mathcal{R}^{\text{sparse}}$  with the terminal heuristic sampling policy  $\pi_T^h$  for the sparse-reward POMDP, it may not help to pre-train with any other heuristic sampling policies for the dense-reward POMDP. In particular, previous dynamic sampling methods that utilize the dense-reward POMDP pre-train reconstructors with a mixture of heuristic sampling policy  $\pi_{\text{mix}}^h = \sum_{t=\|\mathbf{M}_0\|_\infty}^{T+\|\mathbf{M}_0\|_\infty} c_t \pi_t^h$  where  $\sum c_t = 1$ . We will empirically show that using  $\pi_{\text{mix}}^h$  for pre-training is worse than using  $\pi_T^h$  in most cases, which is what we call distributional mismatch.

**Remark 2.** The additional assumption that ' $\forall \mathbf{a}$  that  $\|\mathbf{a}\|_1 = T_+$  satisfies  $\pi_{T_+}^h(\mathbf{a}) > 0$ ' is necessary and easy to achieve in experiments. We leave a counter-example that invalidates the conclusion without the assumption in Appendix B.2.

In addition to improving inference efficiency and eliminating distributional mismatch, the proposed sparse-reward POMDP has one more benefit. It decouples sampling and reconstruction, which makes the sampling trajectories no longer depend on the reconstructor, but only on the sampler and images. This provides a feasible way for solving the sparse-reward joint optimization problem (Eq. (15)).

## 5.2. Alternating Training Framework

In this subsection, we design an alternating training framework to solve the sparse-reward joint optimization problem Eq. (15).

The reconstructor is pre-trained with a terminal heuristic sampling policy  $\pi_T^h$ . Throughout the training, we alternately train the sampler with the reconstructor fix and train the reconstructor with the sampler fix. Mathematically, we solve the following optimization problems in turn:

$$\theta_{\mathcal{R}}^{(0)} = \operatorname{argmax}_{\theta_{\mathcal{R}}} \mathbb{E}_{\mathbf{x} \sim \mathcal{D}} \mathbb{E}_{\mathbf{a} \sim \pi_T^h} [\ell(\mathcal{R}(\mathbf{M}^{\mathbf{a}} \odot \mathcal{F}(\mathbf{x}); \theta_{\mathcal{R}}), \mathbf{x})] \quad (21)$$

$$\theta_\pi^{(l)} = \operatorname{argmax}_{\theta_\pi} \mathbb{E}_{\mathbf{x} \sim \mathcal{D}} J_T^{\text{sparse}}(\mathbf{x}; \pi(\cdot; \theta_\pi), \mathcal{R}(\cdot; \theta_{\mathcal{R}}^{(l-1)})) \quad (22)$$



$$\theta_{\mathcal{R}}^{(l)} = \operatorname{argmax}_{\theta_{\mathcal{R}}} \mathbb{E}_{\mathbf{x} \sim \mathcal{D}} J_T^{\text{sparse}}(\mathbf{x}; \pi(\cdot; \theta_{\pi}^{(l)}), \mathcal{R}(\cdot; \theta_{\mathcal{R}})) \quad (23)$$

where  $L$  is the number of alternation and  $l = 1, 2, \dots, L$ .

Eq. (21) is a standard DL-based MRI reconstruction problem. We train the reconstructor with Adam [13] optimizer.

Eq. (22) can be solved with the proposed sparse-reward POMDP via RL. We use A2C algorithm [18], with a discount factor equal to 1 and a large entropy coefficient to encourage exploring because of the sparse-reward characteristic.

Thanks to the proposed sparse-reward POMDP decoupling sampling and reconstruction, Eq. (23) can be solved by BP. The following proposition allows training the reconstructor with a fixed sampler via gradient-based methods like Adam optimizer.

**Proposition 1** *The derivative of  $J^{\text{sparse}}$  w.r.t.  $\theta_{\mathcal{R}}$  is*

$$\nabla_{\theta_{\mathcal{R}}} J^{\text{sparse}}(\mathbf{x}, \theta) = \mathbb{E}_{\{a_t\}_{t=0}^{T-1} \sim \pi} [\nabla_{\theta_{\mathcal{R}}} \ell(\mathbf{x}_T, \mathbf{x} \mid \mathbf{M}_0, \{a_t\}_{t=0}^{T-1})] \quad (24)$$

where  $\{a_t\}_{t=0}^{T-1} \sim \pi$  means a sequential acquisition with  $\pi$  from the ground truth  $\mathbf{x}$ .

The proof is left in Appendix B.3.

This proposition demonstrates that the loss function of  $\theta_{\mathcal{R}}$  can be calculated by the following three steps. Firstly, we sample  $\mathbf{y}_T$  with the learned policy  $\pi$  from the ground truth  $\mathbf{x}$ . Secondly, we reconstruct  $\mathbf{x}_T = \mathcal{R}(\mathbf{y}_T)$ . Thirdly, we calculate the similarity of the reconstruction image and the ground truth.

We refer to the entire training process as L2SR and summarize it in Algorithm 1.

**Remark.** The proposed alternating training framework is not suitable for the dense-reward POMDP, since there is not a similar derivative of  $J^{\text{dense}}$  w.r.t  $\theta_{\mathcal{R}}$  like Proposition 1. We explain this in more detail in Appendix B.4.

## 6. Experiments

### 6.1. Implementation

**Setup:** We validate our methods under two different settings. One is 'Fixed Reconstructor', which means sampling policies with a fixed reconstructor pre-trained with a heuristic sampling policy. We utilize the proposed sparse-reward POMDP for dynamic sampling to learn a sampler by A2C algorithm, called **L2S** which is short for Learning to Sample. The other is 'Jointly Training', which means the setting of jointly training the sampler and the reconstructor. We utilize the proposed **L2SR**. We refer to Appendix C for more training details on L2S and L2SR.

**Acquisition:** We define the *acceleration factor* as  $N/\|\mathbf{a}\|_1 (\geq 1)$  to measure the time overhead of sampling, denoted as  $(N/\|\mathbf{a}\|_1)$ -acceleration. Most sampling policies

---

### Algorithm 1 Learning to Sampler and Reconstruct (L2SR)

---

**Require:** a sampler  $\pi$ , a reconstructor  $\mathcal{R}$ , a heuristic sampling policy  $\pi^h$ , an MRI dataset  $\mathcal{D}$

- 1: **repeat**
  - 2: sample a batch  $\{\mathbf{x}^{(b)}\}_{b=1}^B \sim \mathcal{D}$  and binary mask vectors  $\mathbf{a}^{(b)} \sim \pi^h$
  - 3:  $\mathcal{L}(\theta_{\mathcal{R}}) = -\frac{1}{B} \sum_{b=1}^B \ell(\mathcal{R}(\mathbf{M}^{\mathbf{a}^{(b)}} \mathcal{F}\mathbf{x}^{(b)}; \theta_{\mathcal{R}}), \mathbf{x}^{(b)})$
  - 4: optimize  $\theta_{\mathcal{R}}$  with the loss  $\mathcal{L}$  by Adam
  - 5: **until** convergence
  - 6: **repeat**
  - 7: build environment (sparse-reward POMDP)
  - 8: train sampler  $\pi$  with the environment by A2C
  - 9: **repeat**
  - 10: sample a batch  $\{\mathbf{x}^{(b)}\}_{b=1}^B \sim \mathcal{D}$  and corresponding acquisition sequences  $\mathbf{a}^{(b)} \sim \pi(\mathbf{x}^{(b)})$
  - 11:  $\mathcal{L}(\theta_{\mathcal{R}}) = -\frac{1}{B} \sum_{b=1}^B \ell(\mathcal{R}(\mathbf{M}^{\mathbf{a}^{(b)}} \mathcal{F}\mathbf{x}^{(b)}; \theta_{\mathcal{R}}), \mathbf{x}^{(b)})$
  - 12: optimize  $\theta_{\mathcal{R}}$  with the loss  $\mathcal{L}$  by Adam
  - 13: **until** convergence
  - 14: **until** convergence
  - 15: Output sampler  $\pi$  and reconstructor  $\mathcal{R}$
- 

first sample a certain number of columns at the central low-frequency region since the low-frequency part of k-space contains more information, and then sample the rest according to their unique strategy. We define the *initial acceleration factor* as the ratio between  $N$  and the number of sampling columns in the first state. We consider  $\times 4$ -acceleration with two initial acceleration factors 8 and 32,  $\times 8$ -acceleration with two initial acceleration factors 16 and 64, and  $\times 16$ -acceleration with two initial acceleration factors 32 and 128. The smaller initial acceleration factor is called *Base-horizon* (or *Base*) and the larger one is called *Long-horizon* (or *Long*) under each acceleration factor.

**Dataset:** We leverage the widely used single-coil knee dataset and multi-coil brain dataset of the fastMRI dataset [36]. All methods are under the same data preprocessing as [2]. We refer to Appendix C.1 for further details.

**Policy model:** We use a CNN-based network with the same architecture as in [2] as the sampler. We refer to Appendix D.1 for further details.

**Reconstruction model:** We use a standard 8-block  $c$ -channel U-Net [22] baseline provided in the fastMRI repository as used in [2], denoted as *Unet-c*. We take the zero-filled reconstruction image  $\mathcal{F}(\mathbf{y}_t)$  as the input of U-net. We refer to Appendix D.2 for further details.

### 6.2. Algorithm Comparisons

For the 'Fixed Reconstructor' setting, we evaluate L2S and compare it with the following three baselines: (1) Random: randomly selecting 1-d lines from a uniform distribu-

		×4-acceleration				×8-acceleration			
		Base-horizon		Long-horizon		Base-horizon		Long-horizon	
		SSIM	PSNR	SSIM	PSNR	SSIM	PSNR	SSIM	PSNR
Fixed Reconstructor	Random+ $\mathcal{R}^{\text{sparse}}$	0.7222 ± 0.0405	26.27 ± 1.78	0.715 ± 0.0329	25.16 ± 1.78	0.6039 ± 0.0492	24.17 ± 1.71	0.5915 ± 0.0442	22.86 ± 2.01
	PG-MRI+ $\mathcal{R}^{\text{dense}}$ [2]	0.7523 ± 0.0375	26.54 ± 1.74	0.7674 ± 0.0299	25.23 ± 1.59	0.623 ± 0.0504	24.21 ± 1.69	0.633 ± 0.0446	23.51 ± 1.74
	L2S+ $\mathcal{R}^{\text{sparse}}$ (Ours)	<b>0.7543 ± 0.0372</b>	<b>26.93 ± 1.79</b>	<b>0.7838 ± 0.0286</b>	<b>26.86 ± 1.68</b>	<b>0.6258 ± 0.0505</b>	<b>24.65 ± 1.72</b>	<b>0.6441 ± 0.0453</b>	<b>24.28 ± 1.71</b>
	Greedy Oracle+ $\mathcal{R}^{\text{dense}}$	0.7658 ± 0.035	26.74 ± 1.75	0.7837 ± 0.0264	25.79 ± 1.7	0.6376 ± 0.0488	24.44 ± 1.71	0.6509 ± 0.043	23.41 ± 1.74
Joint Training	LOUPE [1]	0.7243 ± 0.0387	26.2 ± 1.75	0.72 ± 0.0314	25.09 ± 1.79	0.6002 ± 0.0474	23.96 ± 1.7	0.5876 ± 0.0413	22.64 ± 1.97
	2-Step Seq [35]	0.7612 ± 0.0387	27.18 ± 1.83	0.8025 ± 0.0315	27.69 ± 1.81	0.6336 ± 0.0566	25 ± 1.72	0.6614 ± 0.0508	25.26 ± 1.76
	4-Step Seq [35]	0.7649 ± 0.0408	27.26 ± 1.85	0.7992 ± 0.0331	27.52 ± 1.74	<b>0.6359 ± 0.0572</b>	<b>25.07 ± 1.73</b>	-	-
	L2SR (Ours)	<b>0.7681 ± 0.0416</b>	<b>27.38 ± 1.9</b>	<b>0.8097 ± 0.0333</b>	<b>28.15 ± 1.83</b>	0.6332 ± 0.053	24.98 ± 1.74	<b>0.6712 ± 0.0511</b>	<b>25.61 ± 1.79</b>

Table 1. Reconstruction results (mean and standard deviation) in terms of SSIM and PSNR values on the knee test dataset. We use *Unet-16* as the reconstructor for comparison. For ‘Fixed Reconstructor’, + $\mathcal{R}$  means the heuristic sampling policy for pre-training (see Tab. 5). There is no result for 4-Step Seq under ×8-acceleration and Long-horizon since the number of acquisition step 14 is not a multiple of 4. The best results (highest mean) for a specific acceleration factor and initial acceleration factor among the compared algorithms are shown in bold numbers. The best results for a specific acceleration factor are shown in blue numbers.

		Computational Complexity	Average Inference Time (s)							
			knee dataset		brain dataset					
			×4-acceleration	×8-acceleration	×8-acceleration	×16-acceleration				
			Base	Long	Base	Long	Base	Long	Base	Long
Random & LOUPE	$C_{\mathcal{R}}$		0.004		0.0087					
PG-MRI	$TC_{\pi} + (T + 1)C_{\mathcal{R}}$		0.0843	0.1423	0.0444	0.0727	0.2111	0.3499	0.1011	0.1765
Greedy Oracle	$T(N - \frac{T-1}{2})C_{\mathcal{R}}$		1.2134	2.0440	0.7071	1.1824	4.9728	8.4883	2.7001	4.6615
L2S & L2SR (Ours)	$TC_{\pi} + C_{\mathcal{R}}$		0.0201	0.0325	0.0126	0.0190	0.0390	0.0587	0.0252	0.0360
$\Lambda$ -Step Seq	$\Lambda C_{\pi} + (\Lambda + 1)C_{\mathcal{R}}$		0.0225( $\Lambda = 2$ ), 0.0321( $\Lambda = 4$ )		0.0313( $\Lambda = 2$ ), 0.05( $\Lambda = 4$ )					

Table 2. Comparison of inference costs of different methods. We calculate the computational complexity of sampling and reconstruction required to an MRI scanning.  $C_{\pi}$  and  $C_{\mathcal{R}}$  denote the computational complexity of taking one sample and one reconstruction individually, and  $T$  denotes the length of sampling trajectory, which is  $\frac{N}{\text{initial acceleration factor}} - \frac{N}{\text{acceleration factor}}$ . We also test the average inference time over knee and brain datasets.

tion; (2) PG-MRI<sup>1</sup> [2]: solving the dense-reward POMDP by policy gradient (which is one of the state-of-the-art dynamic sampling methods); (3) Greedy Oracle: one-step oracle policy (having access to ground truth at test time). We use the dense-reward reconstructor  $\mathcal{R}^{\text{dense}}$  pre-trained with a mixture heuristic sampling policy for PG-MRI and Greedy Oracle, and the sparse-reward reconstructor  $\mathcal{R}^{\text{sparse}}$  pre-trained with a terminal heuristic sampling policy for Random and L2R. We refer to Appendix C.1.4 for more details of pre-training. For the ‘Joint Training’ setting, we evaluate L2SR and compare it with the following two baselines: (1) LOUPE [1]: jointly training a learnable non-sequential sampler and a reconstructor; (2)  $\Lambda$ -Step Seq.<sup>2</sup> [35]: end-to-end sequential sampling and reconstruction where  $\Lambda = 2, 4$  (which is the current state-of-the-art). The details of competing methods are left in Appendix E.

### 6.3. Results

We show the SSIM and PSNR values of the reconstructed images of all compared accelerated MRI methods

<sup>1</sup>Thanks for their open source codes on [https://github.com/Timsey/pg\\_mri](https://github.com/Timsey/pg_mri).

<sup>2</sup>Thanks for their open source codes on <https://github.com/tianwei/SeqMRI>. The implementation of LOUPE is also included.

of the knee dataset in Tab. 1 and the histograms at a more granular level in Fig. 1. The results of the brain dataset are left in Appendix F.1. We interpret the results in the following two aspects. As for the ‘Fixed Reconstructor’ setting, L2S achieves the best reconstruction performance in most cases, which shows that eliminating the distributional mismatch provides benefits to reconstruction performances. As for the both two settings, L2SR achieves the best reconstruction performance in most cases, which shows that solving the overall joint optimization problem is better than considering its weakened forms or suboptimization problems.

**Inference Complexity.** Computational complexities during the inference time of trained models are given in Tab. 2. The computational complexity of the proposed L2S and L2SR is lower than PG-MRI and Greedy Oracle. We also show the inference time. L2S and L2SR infer faster than PG-MRI, Greedy Oracle.

**The Best Initial Acceleration Factor.** In practice, we are often more concerned about how to get the best reconstruction for a fixed acceleration factor. Therefore, we take the initial acceleration factor as a hyperparameter and find its optimal value by empirical search. Tab. 3 presents the SSIM values for different initial acceleration factors. It

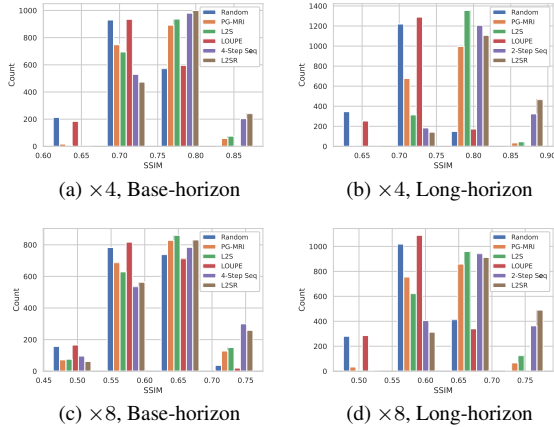


Figure 1. Histograms of SSIM values from the knee test dataset as shown in Tab. 1. Figures in (a), (b), (c) and (d) correspond to the different acceleration factors and initial acceleration factors. Each figure contains histograms of six sampling policies: Random, PG-MRI, L2S, LOUPE,  $\Lambda$ -Step Seq, L2SR.

initial acceleration factor	knee		brain	
	$\times 4$	$\times 8$	$\times 8$	$\times 16$
$N/1$	$0.8055 \pm 0.0327$	$0.6418 \pm 0.0456$	$0.8862 \pm 0.0469$	$0.8385 \pm 0.069$
$N/2$	<b><math>0.8171 \pm 0.0316</math></b>	<b><math>0.6712 \pm 0.0511</math></b>	$0.8911 \pm 0.0452$	$0.8456 \pm 0.0652$
$N/4$	$0.8097 \pm 0.0333$	$0.658 \pm 0.0529$	<b><math>0.8969 \pm 0.0417</math></b>	<b><math>0.8468 \pm 0.0655</math></b>
$N/8$	$0.7999 \pm 0.036$	$0.6332 \pm 0.053$	$0.893 \pm 0.043$	$0.8404 \pm 0.066$
$N/16$	$0.7681 \pm 0.0416$	-	$0.8899 \pm 0.043$	-

Table 3. Empirically searching the best acceleration factors in terms of SSIM values for L2SR. We consider different settings:  $\times 4$  acceleration factor for knee dataset,  $\times 8$  acceleration factor for knee dataset,  $\times 8$  acceleration factor for brain dataset and  $\times 16$  acceleration factor for brain dataset. The best results for each settings are shown in bold numbers.

shows that the proposed L2SR achieves the best reconstruction performance when the initial acceleration factor equals to  $N/2$  for the knee dataset and  $N/4$  for the brain dataset. Although a larger initial acceleration factor will provide the sampler with more degrees of freedom leading to a greater optimal value of Eq. (15), less initial information makes the training more difficult.

**Ablation and Further Discussion.** We further test the transferability of the sparse-reward POMDP, empirically search hyperparameters of L2R and L2SR, and explore the choice of RL algorithms. These supplementary experiments are left in Appendix F.2.

**Visualization.** We visualize an example of the knee dataset in Fig. 2. More visualizations of our methods and competing methods are left in Appendix F.3.

## 7. Conclusion

In this paper, we proposed a joint optimization problem to obtain a personalized sampling policy and its corresponding reconstruction model for accelerated MRI. In particular,

to learn a personalized sampler, we proposed a novel sparse-reward POMDP to formulate the MRI sampling trajectory. Compared to the existing dynamic sampling methods that utilize dense-reward POMDPs, the proposed sparse-reward POMDP is more computationally efficient and has a provable advantage over dense-reward POMDP. Further, we proposed an alternating training framework (called L2SR) to solve the proposed joint optimization problem. We empirically validated the sparse-reward POMDP and L2SR on the fastMRI dataset. By solving the suboptimization problem of learning a sampler with a fixed reconstructor, it shows that the sparse-reward POMDP improves the reconstruction quality by eliminating the distributional mismatch. By solving the joint optimization problem of a pair of samplers and reconstructors, it shows that L2SR achieves the best acceleration-quality trade-off. Additionally, the trained model by L2SR inferences much faster than existing dynamic sampling methods.

There are two limitations of our work. First, the alternating training framework has no theoretic guarantee of convergence. Second, the sparse-reward POMDP requires a well exploratory RL algorithm when solving Eq. (22). However, the RL algorithm we use is not exploratory enough, and thus it is not applicable to the cases with longer sequences or larger action spaces. For future work, other than the aforementioned two aspects, we would like to adapt the proposed L2SR to realistic MRI scanning problems.



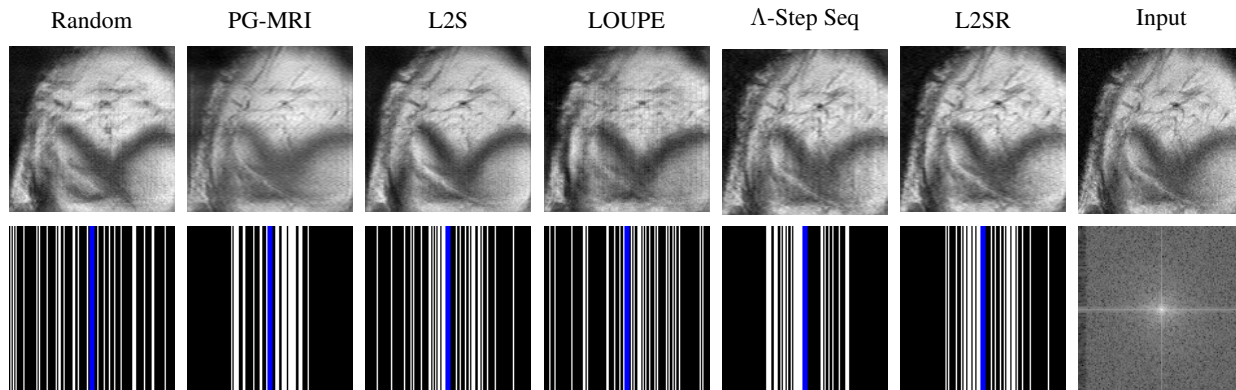


Figure 2. Visualisation of an example of the knee dataset for our methods and other competing methods under  $\times 4$ -acceleration and Long-horizon. From left to right are various accelerated MRI methods: Random, PG-MRI, L2S, LOUPE,  $\Lambda$ -Step Seq, and L2SR; and the last column consisting of ground truth and fully sampled k-space. The first row are reconstruction images of reconstruction images of Long-horizon and the second row is masks of Long-horizon. Measurements sampled from the low-frequency part of k-space in the first state are in blue.

## References

- [1] Cagla Deniz Bahadir, Adrian V Dalca, and Mert R Sabuncu. Learning-based optimization of the under-sampling pattern in mri. In *International Conference on Information Processing in Medical Imaging*, pages 780–792. Springer, 2019. [1](#), [2](#), [7](#), [17](#)
- [2] Tim Bakker, Herke van Hoof, and Max Welling. Experimental design for mri by greedy policy search. In H. Larochelle, M. Ranzato, R. Hadsell, M.F. Balcan, and H. Lin, editors, *Advances in Neural Information Processing Systems*, volume 33, pages 18954–18966. Curran Associates, Inc., 2020. [1](#), [2](#), [6](#), [7](#), [14](#), [15](#), [17](#)
- [3] Jonathan Baxter and Peter L Bartlett. Infinite-horizon policy-gradient estimation. *Journal of Artificial Intelligence Research*, 15:319–350, 2001. [2](#)
- [4] Emmanuel J Candès, Justin Romberg, and Terence Tao. Robust uncertainty principles: Exact signal reconstruction from highly incomplete frequency information. *IEEE Transactions on information theory*, 52(2):489–509, 2006. [1](#)
- [5] Raymond H Chan, Tony F Chan, Lixin Shen, and Zuowei Shen. Wavelet algorithms for high-resolution image reconstruction. *SIAM Journal on Scientific Computing*, 24(4):1408–1432, 2003. [2](#)
- [6] Nicolas Chauffert, Philippe Ciuciu, Jonas Kahn, and Pierre Weiss. Variable density sampling with continuous trajectories. *SIAM Journal on Imaging Sciences*, 7(4):1962–1992, 2014. [2](#)
- [7] Ingrid Daubechies, Michel DeFRise, and Christine De Mol. An iterative thresholding algorithm for linear inverse problems with a sparsity constraint. *Communications on Pure and Applied Mathematics: A Journal Issued by the Courant Institute of Mathematical Sciences*, 57(11):1413–1457, 2004. [2](#)
- [8] Ingrid Daubechies, Ronald DeVore, Massimo Fornasier, and C Sinan Güntürk. Iteratively reweighted least squares minimization for sparse recovery. *Communications on Pure and Applied Mathematics: A Journal Issued by the Courant Institute of Mathematical Sciences*, 63(1):1–38, 2010. [2](#)
- [9] Kerstin Hammernik, Teresa Klatzer, Erich Kobler, Michael P Recht, Daniel K Sodickson, Thomas Pock, and Florian Knoll. Learning a variational network for reconstruction of accelerated mri data. *Magnetic resonance in medicine*, 79(6):3055–3071, 2018. [1](#), [2](#)
- [10] Kurt Hornik, Maxwell Stinchcombe, and Halbert White. Multilayer feedforward networks are universal approximators. *Neural Networks*, 2(5):359–366, 1989. [11](#)
- [11] Chang Min Hyun, Hwa Pyung Kim, Sung Min Lee, Sungchul Lee, and Jin Keun Seo. Deep learning for under-sampled mri reconstruction. *Physics in Medicine & Biology*, 63(13):135007, 2018. [1](#), [2](#)
- [12] Kyong Hwan Jin, Michael Unser, and Kwang Moo Yi. Self-supervised deep active accelerated mri. *arXiv preprint arXiv:1901.04547*, 2019. [1](#), [2](#)
- [13] Diederik P Kingma and Jimmy Ba. Adam: A method for stochastic optimization. *arXiv preprint arXiv:1412.6980*, 2014. [6](#), [15](#), [16](#)
- [14] Dongwook Lee, Jaejun Yoo, Sungho Tak, and Jong Chul Ye. Deep residual learning for accelerated mri using magnitude and phase networks. *IEEE Transactions on Biomedical Engineering*, 65(9):1985–1995, 2018. [1](#), [2](#)
- [15] Yiming Liu, Yanwei Pang, Ruiqi Jin, and Zhenchang Wang. Active phase-encode selection for slice-specific fast mr scanning using a transformer-based deep reinforcement learning framework. *ArXiv*, abs/2203.05756, 2022. [1](#), [2](#)
- [16] Michael Lustig, David Donoho, and John M Pauly. Sparse mri: The application of compressed sensing for rapid mr imaging. *Magnetic Resonance in Medicine: An Official Journal of the International Society for Magnetic Resonance in Medicine*, 58(6):1182–1195, 2007. [1](#), [2](#)
- [17] Michael Lustig, David L Donoho, Juan M Santos, and John M Pauly. Compressed sensing mri. *IEEE signal processing magazine*, 25(2):72–82, 2008. [1](#)

- [18] Volodymyr Mnih, Adria Puigdomenech Badia, Mehdi Mirza, Alex Graves, Timothy Lillicrap, Tim Harley, David Silver, and Koray Kavukcuoglu. Asynchronous methods for deep reinforcement learning. In *International conference on machine learning*, pages 1928–1937. PMLR, 2016. 6
- [19] Luis Pineda, Sumana Basu, Adriana Romero, Roberto Candalra, and Michal Drozdal. Active mr k-space sampling with reinforcement learning. In *International Conference on Medical Image Computing and Computer-Assisted Intervention*, pages 23–33. Springer, 2020. 1, 2
- [20] Tran Minh Quan, Thanh Nguyen-Duc, and Won-Ki Jeong. Compressed sensing mri reconstruction using a generative adversarial network with a cyclic loss. *IEEE Transactions on Medical Imaging*, 37(6):1488–1497, 2018. 1, 2
- [21] Antonin Raffin, Ashley Hill, Adam Gleave, Anssi Kanervisto, Maximilian Ernestus, and Noah Dormann. Stable-baselines3: Reliable reinforcement learning implementations. *Journal of Machine Learning Research*, 22(268):1–8, 2021. 15
- [22] Olaf Ronneberger, Philipp Fischer, and Thomas Brox. U-net: Convolutional networks for biomedical image segmentation. In *International Conference on Medical image computing and computer-assisted intervention*, pages 234–241. Springer, 2015. 6
- [23] Leonid I Rudin, Stanley Osher, and Emad Fatemi. Nonlinear total variation based noise removal algorithms. *Physica D: nonlinear phenomena*, 60(1-4):259–268, 1992. 2
- [24] John Schulman, Filip Wolski, Prafulla Dhariwal, Alec Radford, and Oleg Klimov. Proximal policy optimization algorithms. *arXiv preprint arXiv:1707.06347*, 2017. 18
- [25] Ziju Shen, Yufei Wang, Dufan Wu, Xu Yang, and Bin Dong. Learning to scan: A deep reinforcement learning approach for personalized scanning in ct imaging. *Inverse Problems and Imaging*, 16(1):179–195, 2022. 1, 4
- [26] He Sun, Adrian V. Dalca, and Katherine L. Bouman. Learning a probabilistic strategy for computational imaging sensor selection. In *2020 IEEE International Conference on Computational Photography (ICCP)*, pages 1–12, 2020. 2
- [27] Hans Van Gorp, Iris Huijben, Bastiaan S Veeling, Nicola Pezzotti, and Ruud JG Van Sloun. Active deep probabilistic subsampling. In *International Conference on Machine Learning*, pages 10509–10518. PMLR, 2021. 1, 2
- [28] Hado Van Hasselt, Arthur Guez, and David Silver. Deep reinforcement learning with double q-learning. In *Proceedings of the AAAI conference on artificial intelligence*, volume 30, 2016. 2
- [29] SS Vasawala, MJ Murphy, Marcus T Alley, P Lai, Kurt Keutzer, John M Pauly, and Michael Lustig. Practical parallel imaging compressed sensing mri: Summary of two years of experience in accelerating body mri of pediatric patients. In *2011 IEEE International Symposium on Biomedical Imaging: From nano to macro*, pages 1039–1043. IEEE, 2011. 2
- [30] Guanhua Wang, Tianrui Luo, Jon-Fredrik Nielsen, Douglas C Noll, and Jeffrey A Fessler. B-spline parameterized joint optimization of reconstruction and k-space trajectories (bjork) for accelerated 2d mri. *arXiv preprint arXiv:2101.11369*, 2021. 2
- [31] Zhou Wang, A.C. Bovik, H.R. Sheikh, and E.P. Simoncelli. Image quality assessment: from error visibility to structural similarity. *IEEE Transactions on Image Processing*, 13(4):600–612, 2004. 4, 14
- [32] Tomer Weiss, Sanketh Vedula, Ortal Senouf, Oleg Michailovich, Michael Zibulevsky, and Alex Bronstein. Joint learning of cartesian under sampling andre construction for accelerated mri. In *ICASSP 2020 - 2020 IEEE International Conference on Acoustics, Speech and Signal Processing (ICASSP)*, pages 8653–8657, 2020. 2
- [33] Guang Yang, Simiao Yu, Hao Dong, Greg Slabaugh, Pier Luigi Dragotti, Xujiang Ye, Fangde Liu, Simon Arridge, Jennifer Keegan, Yike Guo, and David Firmin. Dagan: Deep de-aliasing generative adversarial networks for fast compressed sensing mri reconstruction. *IEEE Transactions on Medical Imaging*, 37(6):1310–1321, 2018. 1, 2
- [34] yan yang, Jian Sun, Huibin Li, and Zongben Xu. Deep admm-net for compressive sensing mri. In D. Lee, M. Sugiyama, U. Luxburg, I. Guyon, and R. Garnett, editors, *Advances in Neural Information Processing Systems*, volume 29. Curran Associates, Inc., 2016. 1, 2
- [35] Tianwei Yin, Zihui Wu, He Sun, Adrian V Dalca, Yisong Yue, and Katherine L Bouman. End-to-end sequential sampling and reconstruction for mr imaging. *arXiv preprint arXiv:2105.06460*, 2021. 1, 2, 4, 7, 17
- [36] Jure Zbontar, Florian Knoll, Anuroop Sriram, Tullie Murrell, Zhengnan Huang, Matthew J Muckley, Aaron Defazio, Ruben Stern, Patricia Johnson, Mary Bruno, et al. fastmri: An open dataset and benchmarks for accelerated mri. *arXiv preprint arXiv:1811.08839*, 2018. 2, 6
- [37] Jian Zhang and Bernard Ghanem. Ista-net: Interpretable optimization-inspired deep network for image compressive sensing. In *Proceedings of the IEEE Conference on Computer Vision and Pattern Recognition (CVPR)*, June 2018. 1, 2
- [38] Jinwei Zhang, Hang Zhang, Alan Wang, Qihao Zhang, Mert Sabuncu, Pascal Spincemaille, Thanh D Nguyen, and Yi Wang. Extending loupe for k-space under-sampling pattern optimization in multi-coil mri. In *International Workshop on Machine Learning for Medical Image Reconstruction*, pages 91–101. Springer, 2020. 2
- [39] Zizhao Zhang, Adriana Romero, Matthew J Muckley, Pascal Vincent, Lin Yang, and Michal Drozdal. Reducing uncertainty in undersampled mri reconstruction with active acquisition. In *Proceedings of the IEEE/CVF Conference on Computer Vision and Pattern Recognition*, pages 2049–2058, 2019. 2

## A. Notation Index

Noun	Notation	Reference
image width	$N$	Sec. 3.1
ground truth	$\mathbf{x}$	Sec. 3.1
2D Discrete Fourier Transform	$\mathcal{F}$	Sec. 3.1
fully sampled measurement	$\mathbf{y}$	Sec. 3.1
binary mask matrix	$\mathbf{M}$	Sec. 3.1
observation	$\mathbf{y}$	Sec. 3.1
reconstructor	$\mathcal{R}$	Sec. 3.1
sampler	$\pi$	Sec. 3.1
heuristic sampling policy	$\pi_t^h$	Sec. 3.1
binary mask vector	$\mathbf{a}$	Sec. 3.1
dense-reward POMDP		Sec. 3.1
discount factor	$\gamma$	Sec. 3.1
dense-reward joint optimization problem		Eq. (1) and Eq. (2)
reconstruction suboptimization problem		Eq. (3)
dense-reward suboptimization problem		Eq. (4)
sparse-reward POMDP		Sec. 5.1
sparse-reward joint optimization problem		Eq. (15) and Eq. (16)
sparse-reward suboptimization problem		Eq. (18)
Fixed Reconstructor		Sec. 6.1
Joint Training		Sec. 6.1
acceleration factor		Sec. 6.1
initial acceleration factor		Sec. 6.1
Base-horizon		Sec. 6.1
Long-horizon		Sec. 6.1
Unet-channel	Unet-c	Sec. 6.1

Table 4. Notation index.

## B. Supplements and Proofs for the Theoretic Analysis

### B.1. Proof of Theorem 1

We prove it with Universal Approximation Theorem and dynamic programming.

**Proof (Theorem 1)** Let  $v_{\pi, \mathcal{R}}^{dense}(\mathbf{x}, \mathbf{M}_t)$  and  $v_{\pi, \mathcal{R}}^{sparse}(\mathbf{x}, \mathbf{M}_t)$  be the value function of dense-reward POMDP and sparse-reward POMDP. We define  $v_{\pi, \mathcal{R}}^{dense}(\mathcal{D}, \mathbf{M}_t) = \mathbb{E}_{\mathbf{x} \sim \mathcal{D}} v_{\pi, \mathcal{R}}^{dense}(\mathbf{x}, \mathbf{M}_t)$  and  $v_{\pi, \mathcal{R}}^{sparse}(\mathcal{D}, \mathbf{M}_t) = \mathbb{E}_{\mathbf{x} \sim \mathcal{D}} v_{\pi, \mathcal{R}}^{sparse}(\mathbf{x}, \mathbf{M}_t)$ . Indeed,  $v_{\pi, \mathcal{R}}^{dense}(\mathcal{D}, \mathbf{M}_0)$  is the objective function of Eq. (1) and  $v_{\pi, \mathcal{R}}^{sparse}(\mathcal{D}, \mathbf{M}_0)$  is the objective function of Eq. (15). We want to prove:

$$\max_{\pi, \mathcal{R} \in \mathcal{H}} v_{\pi, \mathcal{R}}^{dense}(\mathcal{D}, \mathbf{M}_0) \leq \max_{\pi, \mathcal{R} \in \mathcal{H}} v_{\pi, \mathcal{R}}^{sparse}(\mathcal{D}, \mathbf{M}_0)$$

For  $\forall \epsilon > 0$ , there exists a pair of continues functions  $\pi^\epsilon$  and  $\mathcal{R}^\epsilon$  satisfying

$$\max_{\pi, \mathcal{R} \in \mathcal{H}} v_{\pi, \mathcal{R}}^{dense}(\mathcal{D}, \mathbf{M}_0) - v_{\pi^\epsilon, \mathcal{R}^\epsilon}^{dense}(\mathcal{D}, \mathbf{M}_0) < \epsilon$$

The **universal approximation theorem** [10] guarantees that there exist  $\pi^*, \mathcal{R}^* \in \mathcal{H}$  for  $\forall \epsilon_\pi > 0$  and  $\forall \epsilon_{\mathcal{R}} > 0$  satisfying

$$\sup_{\mathbf{y} \in \mathbb{C}^{N \times N}} |\mathcal{R}^*(\mathbf{y}) - \mathcal{R}^\epsilon(\mathbf{y})| < \epsilon_{\mathcal{R}}$$

and

$$\sup_{\mathbf{y} \in \mathbb{C}^{N \times N}} |\pi^*(\cdot | \mathbf{y}) - \pi^\epsilon(\cdot | \mathcal{R}^\epsilon(\mathbf{y}))| < \epsilon_\pi$$

We have the recursion formula for both  $v_{\pi, \mathcal{R}}^{dense}(\mathbf{x}, \mathbf{M}_0)$ :

$$v_{\pi, \mathcal{R}}^{dense}(\mathbf{x}, \mathbf{M}_t) = \sum_{a_t=1}^N \pi(a_t | \mathbf{x}_t) \cdot v_{\pi, \mathcal{R}}(\mathbf{x}, \mathbf{M}_t + \mathbf{M}^{a_t}).$$

and  $v_{\pi, \mathcal{R}}^{sparse}(\mathbf{x}, \mathbf{M}_0)$ :

$$v_{\pi, \mathcal{R}}^{sparse}(\mathbf{x}, \mathbf{M}_t) = \sum_{a_t=1}^N \pi(a_t | \mathbf{y}_t) \cdot v_{\pi, \mathcal{R}}(\mathbf{x}, \mathbf{M}_t + \mathbf{M}^{a_t}).$$

Since the similarity metric function  $\ell$  is bounded by  $[0, 1]$ ,  $v_{\pi, \mathcal{R}} \in [0, 1]$ . Recursively, we have

$$\begin{aligned} v_{\pi^\epsilon, \mathcal{R}^\epsilon}^{dense}(\mathcal{D}, \mathbf{M}_T) &= \mathbb{E}_{\mathbf{x} \sim \mathcal{D}} \ell(\mathcal{R}^\epsilon(\mathbf{M}_T \odot \mathcal{F}(\mathbf{x})), \mathbf{x}) \\ &< \mathbb{E}_{\mathbf{x} \sim \mathcal{D}} [\ell(\mathcal{R}^*(\mathbf{M}_T \odot \mathcal{F}(\mathbf{x})), \mathbf{x}) + \epsilon_{\mathcal{R}} \delta] \\ &= v_{\pi^*, \mathcal{R}^*}^{sparse}(\mathcal{D}, \mathbf{M}_T) + \epsilon_{\mathcal{R}} \delta \end{aligned}$$

$$\begin{aligned} &v_{\pi^\epsilon, \mathcal{R}^\epsilon}^{dense}(\mathcal{D}, \mathbf{M}_{T-1}) \\ &= \mathbb{E}_{\mathbf{x} \sim \mathcal{D}} \sum_{a_{T-1}=1}^n \pi^\epsilon(a_{T-1} | \mathbf{x}_{T-1}) \cdot v_{\pi^\epsilon, \mathcal{R}^\epsilon}^{dense}(\mathbf{x}, \mathbf{M}_{T-1} + \mathbf{M}^{a_{T-1}}) \\ &< \mathbb{E}_{\mathbf{x} \sim \mathcal{D}} \sum_{a_{T-1}=1}^n \pi^*(a_{T-1} | \mathbf{y}_{T-1}) \cdot v_{\pi^\epsilon, \mathcal{R}^\epsilon}^{dense}(\mathbf{x}, \mathbf{M}_{T-1} + \mathbf{M}^{a_{T-1}}) + \epsilon_\pi \\ &< \mathbb{E}_{\mathbf{x} \sim \mathcal{D}} \sum_{a_{T-1}=1}^n \pi^*(a_{T-1} | \mathbf{y}_{T-1}) \cdot [v_{\pi^*, \mathcal{R}^*}^{sparse}(\mathbf{x}, \mathbf{M}_{T-1} + \mathbf{M}^{a_{T-1}}) + \epsilon_{\mathcal{R}} \delta] + \epsilon_\pi \\ &= v_{\pi^*, \mathcal{R}^*}^{sparse}(\mathcal{D}, \mathbf{M}_{T-1}) + \epsilon_\pi + \epsilon_{\mathcal{R}} \delta \\ &\dots \end{aligned}$$

Finally, we have

$$v_{\pi^\epsilon}^{dense}(\mathcal{D}, \mathbf{M}_0) < v_{\pi^*}^{sparse}(\mathcal{D}, \mathbf{M}_0) + T\epsilon_\pi + \epsilon_{\mathcal{R}} \delta$$

Because of the arbitrariness of  $\epsilon$ ,  $\epsilon_\pi$  and  $\epsilon_{\mathcal{R}}$ , the proof is completed!

### B.2. Proof of Theorem 2

**Proof (Theorem 2)** Without loss of generality, suppose that  $\mathbf{M} = \mathbf{0}$ , so that  $T_+ = T$ .

We denote

$$J(\mathbf{a}, \mathcal{R}) = \mathbb{E}_{\mathbf{x} \sim \mathcal{D}} \ell(\mathcal{R}(\mathbf{M}^{\mathbf{a}} \odot \mathcal{F}(\mathbf{x})), \mathbf{x})$$

We first prove that for  $\forall \|\mathbf{a}\|_1 = T$ , we have

$$J(\mathbf{a}, \mathcal{R}^{dense}) \leq J(\mathbf{a}, \mathcal{R}^{sparse})$$

by contradiction.

If it does not hold, there  $\exists \|\mathbf{a}^*\|_1 = T$  that

$$J(\mathbf{a}^*, \mathcal{R}^{dense}) > J(\mathbf{a}^*, \mathcal{R}^{sparse})$$

Then, we will prove that it contradicts to the the maximum property of  $\mathcal{R}^{sparse}$ .

Notice that the input of  $\mathcal{R}$  is  $\tilde{\mathbf{y}} = \mathbf{M}^{\mathbf{a}} \odot \mathbf{y}$ , so their exists an injective function  $\mathcal{A} : \mathbb{C}^{N \times N} \rightarrow \{0, 1\}^N, \tilde{\mathbf{y}} \rightarrow \mathbf{a}$ . We define  $\mathcal{Y} : \mathbb{C}^{N \times N} \rightarrow \mathbb{R}^+, \tilde{\mathbf{y}} \rightarrow \min_{\mathcal{A}(\tilde{\mathbf{x}}) = \mathbf{a}} \{\|\mathbf{M}^{\mathbf{a}} \odot \tilde{\mathbf{y}}\|_2\}$  as the minimal norm of the non-zero column of  $\tilde{\mathbf{y}}$ .

We construct a new reconstructor on two disjoint closed subsets of  $\mathbb{C}^{N \times N}$ :

$$\mathcal{R}^{new}(\tilde{\mathbf{y}}) = \begin{cases} \mathcal{R}^{sparse}, & \|\mathcal{A}(\tilde{\mathbf{y}})\|_1 \leq T \text{ and } \mathcal{A}(\tilde{\mathbf{y}}) \neq \mathbf{a}^* \\ \mathcal{R}^{dense}, & \mathcal{A}(\tilde{\mathbf{y}}) = \mathbf{a}^* \text{ and } \mathcal{Y}(\tilde{\mathbf{y}}) \geq \epsilon \end{cases}$$

where  $\epsilon > 0$  is pending. (We give a supplementary description for the convenience of understanding: the constrain of the second term  $\mathcal{Y}(\tilde{\mathbf{y}}) \geq \epsilon$  is just for continuity.) Then, we further extent the domain of  $\mathcal{R}^{new}$  to  $\mathbb{C}^{N \times N}$  by Tietze extension theorem, denoted as  $\mathcal{R}^{New} : \mathbb{C}^{N \times N} \rightarrow \mathbb{R}^{N \times N} \in \mathcal{C}$ .

Finally, we will verify that  $\mathcal{R}^{New}$  is better than  $\mathcal{R}^{sparse}$ , that is

$$\mathbb{E}_{\mathbf{a} \sim \pi_T^h} J(\mathbf{a}, \mathcal{R}^{sparse}) < \mathbb{E}_{\mathbf{a} \sim \pi_T^h} J(\mathbf{a}, \mathcal{R}^{New})$$

which contradicts to the maximum property.

Since  $\pi_T^h(\mathbf{a}^*) > 0$ , we only need to verify that

$$J(\mathbf{a}^*, \mathcal{R}^{sparse}) < J(\mathbf{a}^*, \mathcal{R}^{New})$$

Indeed, we choose a sufficiently small  $\epsilon$  satisfying

$$\begin{aligned} & \mathbb{E}_{\mathbf{x} \sim \mathcal{D}} \mathbb{1}_{\{\mathcal{Y}(\mathbf{M}^{\mathbf{a}^*} \mathcal{F}\mathbf{x}) \geq \epsilon\}} \cdot \\ & \left[ \ell(\mathcal{R}^{dense}(\mathbf{M}^{\mathbf{a}^*} \mathcal{F}\mathbf{x}), x) - \ell(\mathcal{R}^{sparse}(\mathbf{M}^{\mathbf{a}^*} \mathcal{F}\mathbf{x}), x) \right] \\ & > \frac{2}{3} (J(\mathbf{a}^*, \mathcal{R}^{dense}) - J(\mathbf{a}^*, \mathcal{R}^{sparse})) \end{aligned}$$

and

$$\mathbb{E}_{\mathbf{x} \sim \mathcal{D}} \mathbb{1}_{\{\mathcal{Y}(\mathbf{M}^{\mathbf{a}^*} \mathcal{F}\mathbf{x}) < \epsilon\}} < \frac{1}{3} (J(\mathbf{a}^*, \mathcal{R}^{dense}) - J(\mathbf{a}^*, \mathcal{R}^{sparse}))$$

Then, we have

$$\begin{aligned} & J(\mathbf{a}^*, \mathcal{R}^{New}) - J(\mathbf{a}^*, \mathcal{R}^{sparse}) \\ &= \mathbb{E}_{\mathbf{x} \sim \mathcal{D}} \left[ \ell(\mathcal{R}^{New}(\mathbf{M}^{\mathbf{a}^*} \mathcal{F}\mathbf{x}), x) - \ell(\mathcal{R}^{sparse}(\mathbf{M}^{\mathbf{a}^*} \mathcal{F}\mathbf{x}), x) \right] \\ &= \mathbb{E}_{\mathbf{x} \sim \mathcal{D}} \mathbb{1}_{\{\mathcal{Y}(\mathbf{M}^{\mathbf{a}^*} \mathcal{F}\mathbf{x}) \geq \epsilon\}} \cdot \\ & \quad \left[ \ell(\mathcal{R}^{dense}(\mathbf{M}^{\mathbf{a}^*} \mathcal{F}\mathbf{x}), x) - \ell(\mathcal{R}^{sparse}(\mathbf{M}^{\mathbf{a}^*} \mathcal{F}\mathbf{x}), x) \right] \\ & \quad + \mathbb{E}_{\mathbf{x} \sim \mathcal{D}} \mathbb{1}_{\{\mathcal{Y}(\mathbf{M}^{\mathbf{a}^*} \mathcal{F}\mathbf{x}) < \epsilon\}} \cdot \\ & \quad \left[ \ell(\mathcal{R}^{New}(\mathbf{M}^{\mathbf{a}^*} \mathcal{F}\mathbf{x}), x) - \ell(\mathcal{R}^{sparse}(\mathbf{M}^{\mathbf{a}^*} \mathcal{F}\mathbf{x}), x) \right] \\ &\geq \mathbb{E}_{\mathbf{x} \sim \mathcal{D}} \mathbb{1}_{\{\mathcal{Y}(\mathbf{M}^{\mathbf{a}^*} \mathcal{F}\mathbf{x}) \geq \epsilon\}} \cdot \\ & \quad \left[ \ell(\mathcal{R}^{dense}(\mathbf{M}^{\mathbf{a}^*} \mathcal{F}\mathbf{x}), x) - \ell(\mathcal{R}^{sparse}(\mathbf{M}^{\mathbf{a}^*} \mathcal{F}\mathbf{x}), x) \right] \\ & \quad - \mathbb{E}_{\mathbf{x} \sim \mathcal{D}} \mathbb{1}_{\{\mathcal{Y}(\mathbf{M}^{\mathbf{a}^*} \mathcal{F}\mathbf{x}) < \epsilon\}} \\ &> \left( \frac{2}{3} - \frac{1}{3} \right) (J(\mathbf{a}^*, \mathcal{R}^{dense}) - J(\mathbf{a}^*, \mathcal{R}^{sparse})) \\ &= \frac{1}{3} (J(\mathbf{a}^*, \mathcal{R}^{dense}) - J(\mathbf{a}^*, \mathcal{R}^{sparse})) \\ &> 0 \end{aligned}$$

Therefore, it is contradicts to the maximum property of  $\mathcal{R}^{sparse}$ . Therefore, for  $\forall \|\mathbf{a}\|_1 = T$ ,

$$J(\mathbf{a}, \mathcal{R}^{dense}) \leq J(\mathbf{a}, \mathcal{R}^{sparse})$$

The rest of the proof is similar to the proof of Theorem 1. Let  $v_{\pi}^{dense}(\mathbf{x}, \mathbf{M}_t)$  and  $v_{\pi}^{sparse}(\mathbf{x}, \mathbf{M}_t)$  be the value function of dense-reward POMDP and sparse-reward POMDP. We define  $v_{\pi}^{dense}(\mathcal{D}, \mathbf{M}_t) = \mathbb{E}_{\mathbf{x} \sim \mathcal{D}} v_{\pi}^{dense}(\mathbf{x}, \mathbf{M}_t)$  and  $v_{\pi}^{sparse}(\mathcal{D}, \mathbf{M}_t) = \mathbb{E}_{\mathbf{x} \sim \mathcal{D}} v_{\pi}^{sparse}(\mathbf{x}, \mathbf{M}_t)$ . Indeed,  $v_{\pi}^{dense}(\mathcal{D}, \mathbf{M}_0)$  is the objective function of Eq. (4) and  $v_{\pi}^{sparse}(\mathcal{D}, \mathbf{M}_0)$  is the objective function of Eq. (18). We want to prove:

$$\max_{\pi \in \mathcal{H}} v_{\pi}^{dense}(\mathcal{D}, \mathbf{M}_0) \leq \max_{\pi \in \mathcal{H}} v_{\pi}^{sparse}(\mathcal{D}, \mathbf{M}_0)$$

For  $\forall \epsilon > 0$ , there exists a sampler  $\pi^{\epsilon}$  satisfying

$$\max_{\pi} v_{\pi}^{dense}(\mathcal{D}, \mathbf{M}_0) - v_{\pi^{\epsilon}}^{dense}(\mathcal{D}, \mathbf{M}_0) < \epsilon$$

The universal approximation theorem guarantees that there exist  $\pi^*$  for  $\forall \epsilon_{\pi} > 0$  which satisfies

$$\sup_{\mathbf{y} \in \mathbb{C}^{N \times N}} |\pi^*(\cdot | \mathbf{y}) - \pi^{\epsilon}(\cdot | \mathcal{R}^{dense}(\mathbf{y}))| < \epsilon_{\pi}$$

We have the recursion formula for both  $v_{\pi}^{dense}(\mathbf{x}, \mathbf{M}_0)$ :

$$v_{\pi}^{dense}(\mathbf{x}, M_t) = \sum_{a_t=1}^N \pi(a_t | \mathbf{x}_t) \cdot v_{\pi}(\mathbf{x}, \mathbf{M}_t + \mathbf{M}^{a_t}).$$

and  $v_{\pi}^{sparse}(\mathbf{x}, \mathbf{M}_0)$ :

$$v_{\pi}^{sparse}(\mathbf{x}, M_t) = \sum_{a_t=1}^N \pi(a_t | \mathbf{y}_t) \cdot v_{\pi, \mathcal{R}}(\mathbf{x}, \mathbf{M}_t + \mathbf{M}^{a_t}).$$

Since the similarity metric function  $\ell$  is bounded by  $[0, 1]$ ,  $v_\pi \in [0, 1]$ . Recursively, we have

$$\begin{aligned} v_{\pi^\epsilon}^{\text{dense}}(\mathcal{D}, \mathbf{M}_T) &= \mathbb{E}_{\mathbf{x} \sim \mathcal{D}} \ell(\mathcal{R}^{\text{dense}}(\mathbf{M}_T \odot \mathcal{F}(\mathbf{x})), \mathbf{x}) \\ &\leq \mathbb{E}_{\mathbf{x} \sim \mathcal{D}} [\ell(\mathcal{R}^{\text{sparse}}(\mathbf{M}_T \odot \mathcal{F}(\mathbf{x})), \mathbf{x})] \\ &= v_{\pi^*}^{\text{sparse}}(\mathcal{D}, \mathbf{M}_T) \end{aligned}$$

$$\begin{aligned} &v_{\pi^\epsilon}^{\text{dense}}(\mathcal{D}, \mathbf{M}_{T-1}) \\ &= \mathbb{E}_{\mathbf{x} \sim \mathcal{D}} \sum_{a_{T-1}=1}^n \pi^\epsilon(a_t | \mathbf{x}_{T-1}) \cdot v_{\pi^\epsilon}^{\text{dense}}(\mathbf{x}, \mathbf{M}_{T-1} + \mathbf{M}^{a_{T-1}}) \quad \text{and} \\ &< \mathbb{E}_{\mathbf{x} \sim \mathcal{D}} \sum_{a_{T-1}=1}^n \pi^*(a_t | \mathbf{y}_{T-1}) \cdot v_{\pi^\epsilon}^{\text{dense}}(\mathbf{x}, \mathbf{M}_{T-1} + \mathbf{M}^{a_{T-1}}) + \epsilon_\pi \\ &\leq \mathbb{E}_{\mathbf{x} \sim \mathcal{D}} \sum_{a_t=1}^n \pi^*(a_t | \mathbf{y}_{T-1}) \cdot [v_{\pi^*}^{\text{sparse}}(\mathbf{x}, \mathbf{M}_{T-1} + \mathbf{M}^{a_{T-1}})] + \epsilon_\pi \\ &= v_{\pi^*}^{\text{sparse}}(\mathcal{D}, \mathbf{M}_{T-1}) + \epsilon_\pi \end{aligned}$$

...

Finally, we have

$$v_{\pi^\epsilon}^{\text{dense}}(\mathcal{D}, \mathbf{M}_0) < v_{\pi^*}^{\text{sparse}}(\mathcal{D}, \mathbf{M}_0) + T\epsilon_\pi$$

Because of the arbitrariness of  $\epsilon$  and  $\epsilon_\pi$ , the proof is completed!

**Remark.** Next, we briefly show a counter-example without the additional assumption that ' $\forall \mathbf{a}$  that  $\|\mathbf{a}\|_1 = T_+$  satisfies  $\pi_{T_+}(\mathbf{a}) > 0$ '. Similarly, we suppose that  $\mathbf{M} = \mathbf{0}$ , so  $T_+ = T$ . Suppose that there exists  $\mathbf{a}^*$  that  $\|\mathbf{a}^*\|_1 = T$  which satisfies  $\pi_T(\mathbf{a}^*) = 0$ . Let dataset  $\mathcal{D} = \{\mathbf{x}\}$ , where  $\mathbf{M}^{\mathbf{a}^*} \odot \mathcal{F}(\mathbf{x}) \neq \mathbf{0}$  and  $\mathbf{M}^{1-\mathbf{a}^*} \odot \mathcal{F}(\mathbf{x}) > \mathbf{0}$ . Then, let  $\mathcal{R}^{\text{sparse}}$  be the solution of the optimization problem Eq. (19). Moreover, let  $\mathcal{R}^{\text{dense}}(\mathbf{M}^{\mathbf{a}^*} \odot \mathcal{F}(\mathbf{x})) = \mathbf{x}$  and  $\mathcal{R}^{\text{sparse}}(\mathbf{M}^{\mathbf{a}^*} \odot \mathcal{F}(\mathbf{x})) = \mathbf{0}$ . The construction in the above proof guarantees the continuity of the two reconstructors. Therefore, that  $\pi^{\text{dense}} = \mathbf{a}^*$  makes the L.H.S of Eq. (20) equal to 1. However,  $\mathcal{R}^{\text{sparse}}$  can not do reconstruction perfectly which makes the R.H.S of Eq. (20) smaller than 1.

### B.3. Proof of Proposition 1

We prove it with the idea of dynamic programming.

**Proof (Proposition 1)** Here we consider the sparse-reward POMDP. Let  $v(\mathbf{x}, \mathbf{M}_t)$  be the value function and  $q(\mathcal{R}(\mathbf{y}_t), a_t)$  be the Q function, which is defined as

$$\begin{aligned} v(\mathbf{x}, \mathbf{M}_t) &= \mathbb{E}_{\{a_s\}_{s=t}^{T-1} \sim \pi} r_T \\ q(\mathbf{y}_t, a_t) &= r_{t+1} + v(\mathbf{x}, \mathbf{M}_{t+1}) \end{aligned}$$

Indeed,

$$J^{\text{sparse}}(\mathbf{x}) = v(\mathbf{x}, \mathbf{M}_0)$$

For  $t = 0, 1, \dots, T-1$ , we have

$$\begin{aligned} \nabla_{\theta_{\mathcal{R}}} v(\mathbf{x}, \mathbf{M}_t) &= \nabla_{\theta_{\mathcal{R}}} \left[ \sum_{a_t} \pi(a_t | \mathbf{y}_t) \cdot q(\mathbf{y}_t, a_t) \right] \\ &= \sum_{a_t} [\nabla_{\theta_{\mathcal{R}}} \pi \cdot q_t + \pi \cdot \nabla_{\theta_{\mathcal{R}}} q_t] \\ &= \sum_{a_t} \pi \cdot \nabla_{\theta_{\mathcal{R}}} (r_{t+1} + v(\mathbf{x}, \mathbf{M}_{t+1})) \end{aligned}$$

$$\nabla_{\theta_{\mathcal{R}}} v(\mathbf{x}, \mathbf{M}_T) = 0$$

where  $r_t = 0$  ( $t = 1, \dots, T-1$ ) and  $r_T = \ell(\mathcal{R}(\mathbf{y}_T), x | \mathbf{M}_0, \{a_t\}_{t=0}^{T-1})$ .

Finally, we have

$$\begin{aligned} &\nabla_{\theta_{\mathcal{R}}} J^{\text{sparse}}(\mathbf{x}, \theta) \\ &= \sum_{a_0, \dots, a_{T-1}} \Pr(\mathbf{y}_0 \xrightarrow{\{a_t\}_{t=0}^{T-1}} \mathbf{y}_T, \pi) \\ &\quad \cdot \nabla_{\theta_{\mathcal{R}}} \ell(\mathcal{R}(\mathbf{y}_T), \mathbf{x} | \mathbf{M}_0, \{a_t\}_{t=0}^{T-1}) \\ &= \mathbb{E}_{\{a_t\}_{t=0}^{T-1} \sim \pi} [\nabla_{\theta_{\mathcal{R}}} \ell(\mathbf{x}_T, \mathbf{x} | \mathbf{M}_0, \{a_t\}_{t=0}^{T-1})] \end{aligned}$$

### B.4. alternate Training for Dense-reward POMDP Fails

We will demonstrate that the proposed alternate training framework is not suitable for the dense-reward POMDP. We start by calculating the derivative of  $J^{\text{dense}}$  w.r.t the  $\theta_{\mathcal{R}}$ .

**Proposition 2** The derivative of  $J^{\text{dense}}$  w.r.t.  $\theta_{\mathcal{R}}$  is

$$\begin{aligned} &\nabla_{\theta_{\mathcal{R}}} J^{\text{dense}}(\mathbf{x}, \theta) \\ &= \sum_{t=0}^{T-1} \mathbb{E}_{\{a_s\}_{s=0}^{t-1} \sim \pi} \left[ \sum_{a_t} \nabla_{\theta_{\mathcal{R}}} \pi(a_t | \mathcal{R}(\tilde{\mathbf{x}}_t)) \cdot q_t \right] \quad (25) \\ &\quad + \mathbb{E}_{\{a_t\}_{t=0}^{T-1} \sim \pi} [\nabla_{\theta_{\mathcal{R}}} \ell(\mathbf{x}_T, \mathbf{x} | \mathbf{M}_0, \{a_t\}_{t=0}^{T-1})] \end{aligned}$$

where  $q_t = q(\mathbf{x}_t, a_t)$  is the Q-function of the dense-reward POMDP.

**Proof (Proposition 2)** Here we consider the dense-reward POMDP. Let  $v(\mathbf{x}, \mathbf{M}_t)$  be the value function and  $q(\mathcal{R}(\mathbf{y}_t), a_t)$  be the Q function, defined as

$$v(\mathbf{x}, \mathbf{M}_t) = \mathbb{E}_{\{a_s\}_{s=t}^{T-1} \sim \pi} \sum_{s=t+1}^T r_s$$

$$q(\mathcal{R}(\mathbf{y}_t), a_t) = r_{t+1} + v(\mathbf{x}, \mathbf{M}_{t+1})$$

Indeed,

$$J^{\text{dense}}(\mathbf{x}) = v(\mathbf{x}, \mathbf{M}_0) + \ell(\mathcal{R}(\mathbf{y}_0), \mathbf{x})$$



For  $t = 0, 1, \dots, T-1$ , we have

$$\begin{aligned}
& \nabla_{\theta_{\mathcal{R}}} v(\mathbf{x}, \mathbf{M}_t) \\
&= \nabla_{\theta_{\mathcal{R}}} \left[ \sum_{a_0} \pi(a_t | \mathcal{R}(\mathbf{y}_t)) \cdot q(\mathcal{R}(\mathbf{y}_t), a_0) \right] \\
&= \sum_{a_t} [\nabla_{\theta_{\mathcal{R}}} \pi \cdot q_t + \pi \cdot \nabla_{\theta_{\mathcal{R}}} q_t] \\
&= \sum_{a_t} [\nabla_{\theta_{\mathcal{R}}} \pi \cdot q_t + \pi \cdot \nabla_{\theta_{\mathcal{R}}} (r_{t+1} + v(\mathbf{x}, \mathbf{M}_{t+1}))] \\
&= \sum_{a_t} [\nabla_{\theta_{\mathcal{R}}} \pi \cdot q_t + \\
&\quad \pi \cdot \nabla_{\theta_{\mathcal{R}}} (\ell(\mathcal{R}(\mathbf{y}_t | \mathbf{M}_0, \{a_s\}_{s=0}^t), \mathbf{x}) + v(\mathbf{x}, \mathbf{M}_{t+1}))] \\
&\quad - \nabla_{\theta_{\mathcal{R}}} \ell(\mathcal{R}(\mathbf{y}_t | \mathbf{M}_0, \{a_s\}_{s=0}^{t-1}), \mathbf{x})
\end{aligned}$$

and

$$\nabla_{\theta_{\mathcal{R}}} v(\mathbf{x}, \mathbf{M}_T) = 0$$

Finally, we have

$$\begin{aligned}
& \nabla_{\theta_{\mathcal{R}}} J^{\text{dense}}(\mathbf{x}, \theta) \\
&= \sum_{t=0}^{T-1} \sum_{a_0, \dots, a_{t-1}} \Pr(\mathbf{y}_0 \xrightarrow{\{a_s\}_{s=0}^{t-1}} \mathbf{y}_t, \pi) \\
&\quad \cdot \left[ \sum_{a_t} \nabla_{\theta_{\mathcal{R}}} \pi(a_t | \mathcal{R}(\mathbf{y}_t)) \cdot q_t \right] \\
&\quad + \sum_{a_0, \dots, a_{T-1}} \Pr(\mathbf{y}_0 \xrightarrow{\{a_s\}_{s=0}^{T-1}} \mathbf{y}_T, \pi) \\
&\quad \cdot \nabla_{\theta_{\mathcal{R}}} \ell(\mathbf{x}_T, \mathbf{x} | \mathbf{M}_0, \{a_t\}_{t=0}^{T-1}) \\
&= \sum_{t=0}^{T-1} \mathbb{E}_{\{a_s\}_{s=0}^{t-1} \sim \pi} \left[ \sum_{a_t} \nabla_{\theta_{\mathcal{R}}} \pi(a_t | \mathcal{R}(\mathbf{y}_t)) \cdot q_t \right] \\
&\quad + \mathbb{E}_{\{a_t\}_{t=0}^{T-1} \sim \pi} [\nabla_{\theta_{\mathcal{R}}} \ell(\mathbf{x}_T, \mathbf{x} | \mathbf{M}_0, \{a_t\}_{t=0}^{T-1})]
\end{aligned}$$

The proof is complete!

Although Proposition 2 gives the derivative of dense-reward objective function w.r.t parameters of the reconstructor, we empirically find that training reconstructor with the derivative by gradient-based methods fails. The reason may be that the sequential acquisition  $\{a_t\}_{t=0}^{t-1} \sim \pi$  depends on not only  $\pi$  but also  $\mathcal{R}$ . Changing the reconstructor results to an unpredictable change of the sampling strategy, leading to the failure. From another perspective, the reconstructor can also be viewed as an RL agent, so gradient-based methods hardly work.

## C. Implementation Details of Our Methods

In this section, We will show the implementation details of our methods. In Appendix C.1, we show the basic set-

tings of all algorithms. In Appendix C.2, we show the implementation details of L2R. In Appendix C.3, we show the implementation details of L2SR.

### C.1. Basic Settings

All algorithms, both our methods and competing methods, are performed with the same basic settings as described in this subsection.

#### C.1.1 Data Preprocessing

The data preprocessing is the same as [2]. We always split 20% of the training data into a test set. For the single-coil knee dataset, the ground truth image  $\mathbf{x}$  is obtained by cropping the original ground truth image to the central  $128 \times 128$  region. We use half of the available volumes and remove the outer slices of each volume additionally. This lead to a dataset of 6959 train slices, 1779 validation slices, and 1715 test slices. For the multi-coil brain dataset, the ground truth image  $\mathbf{x}$  is obtained by cropping the original ground truth image to the central  $256 \times 256$  region. We use fifth of the available volumes. This lead to a dataset of 11312 train slices, 4372 validation slices, and 2832 test slices.

#### C.1.2 SSIM Values

SSIM hyperparameters are kept to their original values in [31]. The dynamic range is chosen to be the maximum pixel value in the corresponding ground truth volume.

#### C.1.3 Loss Function

Since the proposed sparse-reward POMDP uses SSIM values as the similarity metric, for consistency, all algorithms use negative SSIM values as a loss.

#### C.1.4 Heuristic Sampling Policy for Pre-training

We use random sampling policy as the heuristic sampling policy to pre-train reconstructors  $\mathcal{R}^{\text{dense}}$  and  $\mathcal{R}^{\text{sparse}}$ . Acceleration factors and initial acceleration factors are shown in Tab. 5. Notice that the choices of heuristic sampling policies for pre-training  $\mathcal{R}^{\text{sparse}}$  are consistent with the assumption of Theorem 2.

## C.2. Implementation of L2R

Dynamic sampling methods have two steps: first pre-training the reconstructor and then training the sampler (as illustrated in Fig. 3a).

We use random policy as the heuristic sampling policy as shown in the above subsection. Training the reconstructor  $\mathcal{R}^{\text{sparse}}$  with the heuristic sampling policy is the same as the competing method **Random**, as detailed in the following section.

×4 acceleration		
	acceleration factor	initial acceleration factor
$\mathcal{R}^{\text{dense}}$	[4,4,4,6,6,8]	[4,6,8,6,8,8]
$\mathcal{R}^{\text{sparse}}$	4	8 (Base) or 32 (Long)
×8 acceleration		
	acceleration factor	initial acceleration factor
$\mathcal{R}^{\text{dense}}$	[8,8,8,12,12,16]	[8,12,16,12,16,16]
$\mathcal{R}^{\text{sparse}}$	8	16 (Base) or 64 (Long)
×16 acceleration		
	acceleration factor	initial acceleration factor
$\mathcal{R}^{\text{dense}}$	[16,16,16,24,24,32]	[16,16,16,24,24,32]
$\mathcal{R}^{\text{sparse}}$	16	32 (Base) or 128 (Long)

Table 5. Acceleration factors and initial accelerations factors of random sampling policies for pre-training reconstructors. We utilize  $\mathcal{R}^{\text{dense}}$  for PG-MRI [2] and Greedy Oracle. We utilize  $\mathcal{R}^{\text{sparse}}$  for Random and L2S.

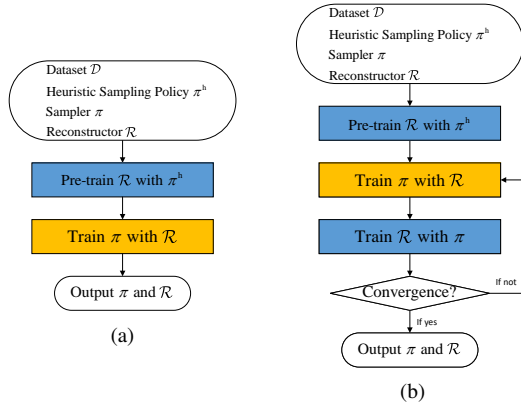


Figure 3. (a) Overview of dynamic sampling training framework. (b) Overview of the proposed alternating training framework.

Building the environment is based on the proposed sparse-reward POMDP with the pre-trained reconstructor. Next, we detail the implementation of the RL algorithm we use here. We implement the A2C algorithm based on the stable-baselines3 [21] which is a popular framework for reliable implementations of RL algorithms. Tab. 6 shows the values of hyperparameters. Hyperparameters not mentioned here are set to default values in the implementation of stable-baselines3.

We refer to the entire training process as L2S and summarize it in Algorithm 2

### C.3. Implementation of Alternate Training

The alternate training framework has two steps: first pre-training the reconstructor and then alternately training the sampler and the reconstructor (as illustrated in Fig. 3b).

The pre-training is also the same as **Random**.

### Algorithm 2 Learning to Sample (L2S)

**Require:** a sampler  $\pi$ , a reconstructor  $\mathcal{R}$ , a heuristic sampling policy  $\pi^h$ , an MRI dataset  $\mathcal{D}$

- 1: **repeat**
- 2: sample a batch  $\{\mathbf{x}^{(b)}\}_{b=1}^B \sim \mathcal{D}$  and binary mask vectors  $\mathbf{a}^{(b)} \sim \pi^h$
- 3:  $\mathcal{L}(\theta_{\mathcal{R}}) = -\frac{1}{B} \sum_{b=1}^B \ell(\mathcal{R}(\mathbf{M}^{\mathbf{a}^{(b)}} \mathcal{F}_{\mathbf{x}^{(b)}}; \theta_{\mathcal{R}}), \mathbf{x}^{(b)})$
- 4: optimize  $\theta_{\mathcal{R}}$  with the loss  $\mathcal{L}$  by Adam
- 5: **until** convergence
- 6: build environment (sparse-reward POMDP)
- 7: train sampler  $\pi$  with the environment by A2C
- 8: Output sampler  $\pi$  and reconstructor  $\mathcal{R}$

Hyperparameter	Value			
	×4		×8	
	Base	Long	Base	Long
optimizer	RMSProp			
learning rate	0.0003			
gamma	1.0			
# parallel environment	16			
entropy coefficient	0.03	0.01	0.003	0.03
update timestep	16	28	8	14
total timestep	40960000			

(a) Hyperparameters for the knee dataset.

Hyperparameter	Value			
	×8		×16	
	Base	Long	Base	Long
optimizer	RMSProp			
learning rate	0.0003			
gamma	1.0			
# parallel environment	4	4	8	8
entropy coefficient	0.03			
update timestep	16	28	8	14
total timestep	40960000			

(b) Hyperparameters for the brain dataset.

Table 6. Hyperparameters of RL training of the L2R algorithm. There is a small trick that we let the 'update timestep' equal to the budget, so that the policy can get accurate values from the sparse-reward POMDP during training.

alternate training does the following two alternate steps: training the sampler with a fixed reconstructor and training the reconstructor with a fixed sampler. The former is the same as the second step of the above dynamic sampling methods that we train the sampler via RL. At the  $l$ th round of training the sampler, we use  $\theta_{\pi}^{(l-1)}$  as initialization, where  $\theta_{\pi}^{(0)}$  is a random initialization. The latter train the reconstructor with the RL-learned policy via Adam [13] optimizer based on Proposition 1. At the  $l$ th round of train-

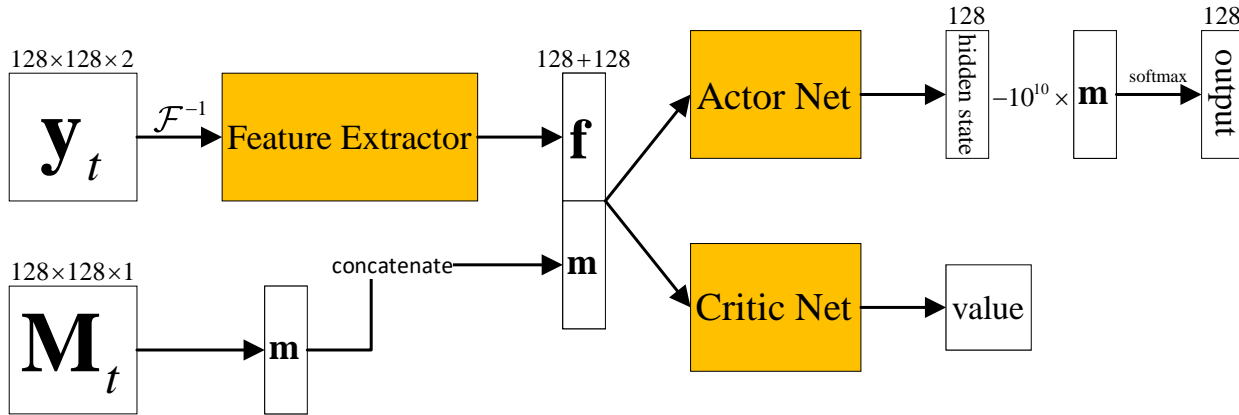


Figure 4. Policy network architecture. Modules in yellow box are parameterized by neural networks, where **Feature Extractor** is a CNN and **Actor Net** and **Critic Net** are both Fully connected neural networks. Modules in yellow are learnable.

Hyperparameter		Value
number of alternate training		5
Train sampler by RL (at the $l(> 1)$ th round)	optimizer	RMSProp
	learning rate	0.001
	# parallel environment	'adaptive'
	entropy coefficient	'adaptive'
	update timestep	'adaptive'
total timestep		8192000
Train reconstructor by BP (at the $l(\geq 1)$ th round)	optimizer	Adam
	batch size	# parallel environment
	num of epochs	10
	learning rate	$0.003/3^{(l-1)}$
	lr step size	5
lr gamma		0.1

Table 7. Hyperparameters of alternating training of the L2SR algorithm. The first round of training sampler by RL is the same as Tab. 6, so we do not show it here. 'adaptive' means that values are equal to the these of the first round of training sampler in Tab. 6.

ing the reconstructor, we use  $\theta_{\mathcal{R}}^{(l-1)}$  as initialization. The entire training process is summarized in Algorithm 1. Tab. 7 shows the values of hyperparameters.

## D. Model Architectures

Both the sampler and the reconstructor are parameterized by neural networks. We show the policy network architecture in Appendix D.1 and the reconstructor network architecture in Appendix D.2.

### D.1. Architecture of Policy Network

We use binary mask matrix  $\mathbf{M}_t$  and the observation  $\mathbf{y}_t = \mathbf{M}_t \odot \mathbf{y}$  as the input of the sampler, that is  $\pi(\cdot | \mathbf{y}_t; \theta_\pi)$  is a discrete probability distributional function.

The sampler network is combined by a 2D Inverse Fourier Transform, a feature extractor, an actor net, and a

critic net, as shown in Fig. 4. The feature extractor is a CNN with the same architecture as the encoder of the Unet-16. It outputs a vector with shape  $(, 128)$  as feature denoted as  $\mathbf{f}$ . The feature is concatenated with a binary mask vector  $\mathbf{m}$  with shape  $(, 128)$  derived by  $\mathbf{M}_t = \mathbf{1} \cdot \mathbf{m}^T$  as the input of the actor net and the critic net. The actor net and the critic net are both fully connected neural networks. The penultimate layer of the actor net outputs a vector with shape  $(, 128)$ , and the last layer of the actor net subtracts  $1e10 \times \mathbf{m}$  from it to prevent the sampler predicting the action that has already been taken. The last layer of the critic net outputs a scalar as the value.

### D.2. Architecture of Reconstruction Network

We use the U-Net baseline provided in the fastMRI repository. The input is the zero-filled reconstruction image  $|\mathcal{F}^{-1}(\mathbf{y}_t)|$  with shape  $(128, 128, 1)$  and the output is the reconstruction image  $\mathbf{x}_t$  with the same shape. There are 8 convolutional blocks and the initial  $(1 \times 1)$  convolution is applied to upsample to  $c$  channels in *Unet-c*.  $c$  is always set as 16 when there is no special statement. The codes are available <sup>3</sup>.

## E. Implementation Details of Competing Methods

In this section, we will show the implementation details of competing methods.

### E.1. Random

We train the reconstructor with random policy by Adam [13] optimizer for 50 epochs. Other hyperparameters inherit

<sup>3</sup><https://github.com/facebookresearch/fastMRI/blob/main/fastmri/models/unet.py>

		×8-acceleration				×16-acceleration			
		Base-horizon		Long-horizon		Base-horizon		Long-horizon	
		SSIM	PSNR	SSIM	PSNR	SSIM	PSNR	SSIM	PSNR
Fixed Reconstructor	Random+ $\mathcal{R}^{\text{sparse}}$	0.8643 ± 0.053	30.66 ± 4.35	0.8405 ± 0.0668	28.65 ± 4.68	80.31 ± 0.0825	27.56 ± 5.03	0.7837 ± 0.0921	26.28 ± 5.02
	PG-MRI+ $\mathcal{R}^{\text{dense}}$ [2]	0.8771 ± 0.0473	31.37 ± 4.18	<b>0.8766 ± 0.0476</b>	<b>31.31 ± 4.17</b>	0.821 ± 0.0722	28.25 ± 4.71	<b>0.8218 ± 0.0721</b>	<b>28.36 ± 4.68</b>
	L2S+ $\mathcal{R}^{\text{sparse}}$ (Ours)	<b>0.8782 ± 0.0475</b>	<b>31.54 ± 4.17</b>	0.8686 ± 0.0529	30.25 ± 4.23	<b>0.8263 ± 0.0703</b>	<b>28.59 ± 4.73</b>	0.819 ± 0.0738	27.65 ± 4.71
	Greedy Oracle+ $\mathcal{R}^{\text{dense}}$	0.8822 ± 0.0453	31.64 ± 4.15	0.8771 ± 0.0532	31.17 ± 4.31	0.8312 ± 0.0677	28.75 ± 4.64	0.8251 ± 0.0734	28.36 ± 4.86
Joint Training	LOUPE [1]	0.8553 ± 0.0555	30.15 ± 4.32	0.8211 ± 0.0691	27.34 ± 3.99	0.8003 ± 0.0821	27.55 ± 4.977	0.7855 ± 0.0894	26.29 ± 4.748
	2-Step Seq [35]	0.8862 ± 0.041	31.93 ± 3.98	0.8921 ± 0.0397	32.07 ± 3.88	0.8291 ± 0.0665	28.95 ± 4.653	0.8384 ± 0.0631	29.34 ± 4.59
	4-Step Seq [35]	0.8857 ± 0.0411	31.86 ± 4.01	0.8854 ± 0.0417	31.76 ± 3.4	0.8314 ± 0.0652	29.05 ± 4.636	-	-
	L2SR (Ours)	<b>0.8899 ± 0.043</b>	<b>32.57 ± 4.09</b>	<b>0.8969 ± 0.0417</b>	<b>32.87 ± 4.02</b>	<b>0.8404 ± 0.066</b>	<b>29.39 ± 4.69</b>	<b>0.8456 ± 0.0652</b>	<b>29.37 ± 4.74</b>

Table 8. Reconstruction results in terms of SSIM ( $\times 100$ ) and PSNR values on the brain test dataset. The best results among the compared algorithms under each settings are shown in bold numbers. The best results for a specific acceleration factor are shown in blue numbers.

the fastMRI repository. We always use early stopping to get the best model on the validation dataset.

## E.2. PG-MRI

We use the best performing  $\gamma = 0.9$  Non-Greedy method in [2]. We train the sampler with its default hyperparameters. The fixed reconstructor is pre-trained by "Random" heuristic sampling policy. Notice that the reconstructor pre-trained is different from [2], since the loss is negative SSIM instead of  $L_1$ -norm and the training dataset is half of the volumes instead of full. In addition, we use early stopping based on the validation set rather than training for the full 50 epochs for better reconstruction performances.

## E.3. Greedy Oracle

The one-step greedy oracle policy has access to the ground truth for reference. We choose the action that will increase similarity the most at test time with a fixed reconstructor the same as above.

## E.4. LOUPE

This method jointly trains the parametric probability mask  $\mathbf{p}$  and the reconstructor end-to-end via BP without pre-training. We use the implementation by [35] and train with its default hyperparameters.

## E.5. $\Lambda$ -Step Seq

This method jointly trains the sampler and the reconstructor end-to-end via BP without pre-training. We train with the the default hyperparameters of [35].

## F. Supplementary Experimental Results

### F.1. Results of Brain Dataset

We show the SSIM and PSNR values of the reconstructed images of all compared accelerated MRI methods of the brain dataset in Tab. 8 and histograms at a more granular level in Fig. 5. We can see that L2SR also achieves the best reconstruction performance. Slightly different from the conclusions in the main text, L2S is a little worse than PG-MRI under Long-horizon. For the reason that brain images

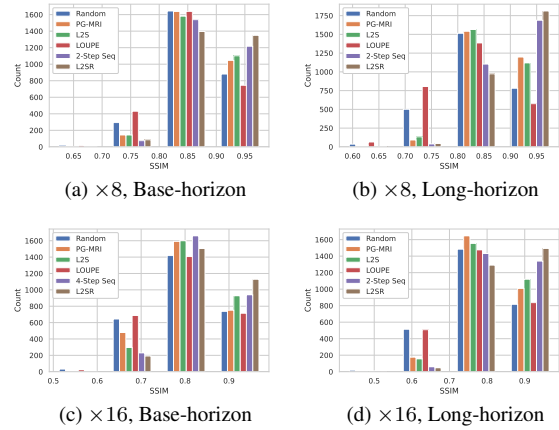


Figure 5. Histograms of SSIM values from the brain test dataset as shown in Tab. 8. Figures in (a), (b), (c) and (d) correspond to the different acceleration factors and initial acceleration factors. Each figure contains histograms of six sampling policies: Random, PG-MRI, L2S, LOUPE,  $\Lambda$ -Step Seq, L2SR.

have twice the resolution of knee images, the initial acceleration factors for  $\mathcal{R}^{\text{sparse}}$  is so small that the random sampler can only sample a small number of informative columns in the central low-frequency region. Reconstructors  $\mathcal{R}^{\text{sparse}}$  pre-trained by such random samplers have poor reconstruction performance (see the results of 'Random').

## F.2. Ablation and Further Discussion

**Transferability.** We first train the sampler with a fixed Unet-16 reconstructor and then evaluate the sampler with fixed Unet-32 and Unet-64 reconstructors pre-trained with the same heuristic sampling policy. Tab. 9 shows the SSIM values of the reconstruction images of random policy and L2S. One can see that the learned sampler can generalize well to the new reconstructors.

**Discount Factor.** Tab. 10 shows how the discount factor makes an impact on the L2S. The reconstruction performance achieves the best when  $\gamma = 1$ , which confirms that policies learned by the proposed sparse-reward POMDP are long-sight.

	Base-horizon		Long-horizon	
	Random	L2S	Random	L2S
Unet-16	0.7222 ± 0.0405	0.7543 ± 0.0372	0.715 ± 0.0329	0.7838 ± 0.0286
Unet-32	0.7238 ± 0.0409	0.7556 ± 0.0374	0.7196 ± 0.0331	0.7844 ± 0.0282
Unet-64	0.7254 ± 0.0409	0.7558 ± 0.0375	0.721 ± 0.0337	0.7856 ± 0.028

Table 9. Transferability of the proposed sparse-reward POMDP. We show SSIM values of our L2S with respect to different reconstruction models under  $\times 4$ -acceleration on the test dataset. Notice that samplers are all trained with pre-trained Unet-16.

	Base-horizon	Long-horizon
$\gamma = 0.5$	0.7129 ± 0.0372	0.7065 ± 0.0298
$\gamma = 0.9$	0.7528 ± 0.0363	0.7826 ± 0.0264
$\gamma = 1.0$	0.7543 ± 0.0372	0.7838 ± 0.0286

Table 10. Influence of discount factor to the proposed sparse-reward POMDP. We show SSIM values of L2S with respect to discount factors under  $\times 4$ -acceleration on the knee test dataset.

Hyperparameter	Value
optimizer	Adam
learning rate	0.001
gamma	1.0
# parallel environment	8
entropy coefficient	0.03
n_steps	2048
K_epochs	10
batch size	128
total timestep	20480000

Table 11. Hyperparameters of PPO algorithm.

**Entropy Coefficient.** Most of the hyperparameters have little effect on RL training and can be set to their default values. It is worth mentioning that our methods are sensitive to the entropy coefficient. A small entropy coefficient will inhibit exploration, leading to poor results, while a large entropy coefficient will overemphasize on exploration which leads to difficulty in convergence. It is difficult for us to give a general guideline for choosing entropy coefficients. Here, we use the validation set to empirically search for the best entropy coefficients.

**RL Algorithms.** It is expected to learn a better sampling policy by some advanced RL algorithms such as PPO [24]. However, we have found that PPO has slow convergence in practice. More specifically, we use hyperparameters shown in Tab. 11 and notice that PPO takes about 5 times as many training steps as A2C. Moreover, PPO slightly improves SSIM values (around 0.001 ~ 0.002). Therefore, we do not use it.

**Number of Alternation.** We use a fixed number of alternation as the stop condition of L2SR. Fig. 6 shows the reconstruction performance with respect to the rounds of

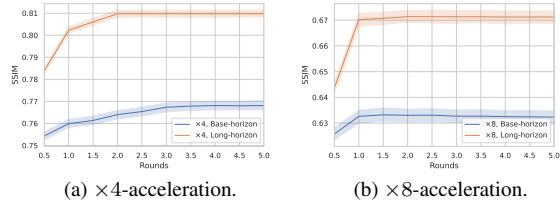


Figure 6. The choice of the number of alternation. We show SSIM values of L2SR with respect to different rounds of alternating training on the knee test dataset. Specifically, "Round =  $l.5$ " means the  $(l + 1)$ th round of training the sampler with the learned reconstructor, and "Round =  $l.0$ " means the  $l$ th round of training the reconstructor with the learned sampler.

alternating training. Usually, it converges within about 5 rounds.

### F.3. More Visualization

More visualizations of our methods and competing methods are shown as follow.



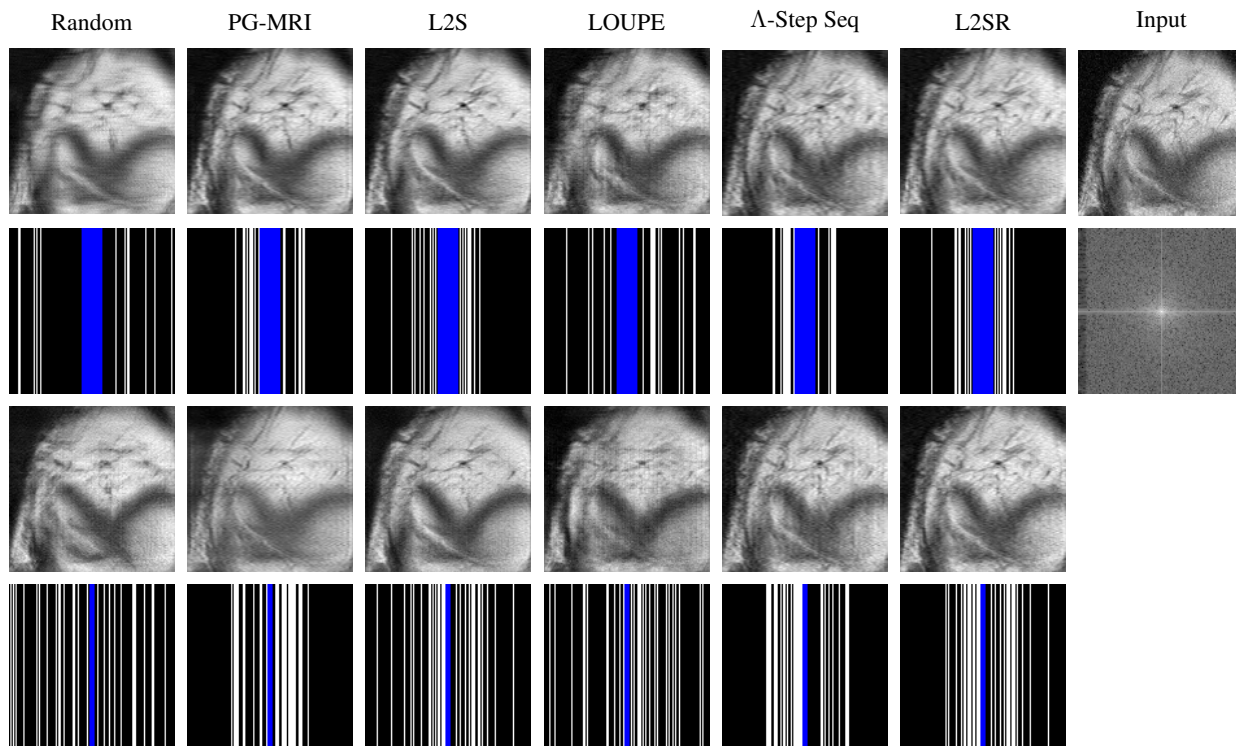


Figure 7. Visualisation of an example of the knee dataset for our methods and other competing methods under  $\times 4$ -acceleration. From top to bottom are reconstruction images of Base-horizon, mask matrices of Base-horizon, reconstruction images of Long-horizon and mask matrices of Long-horizon.

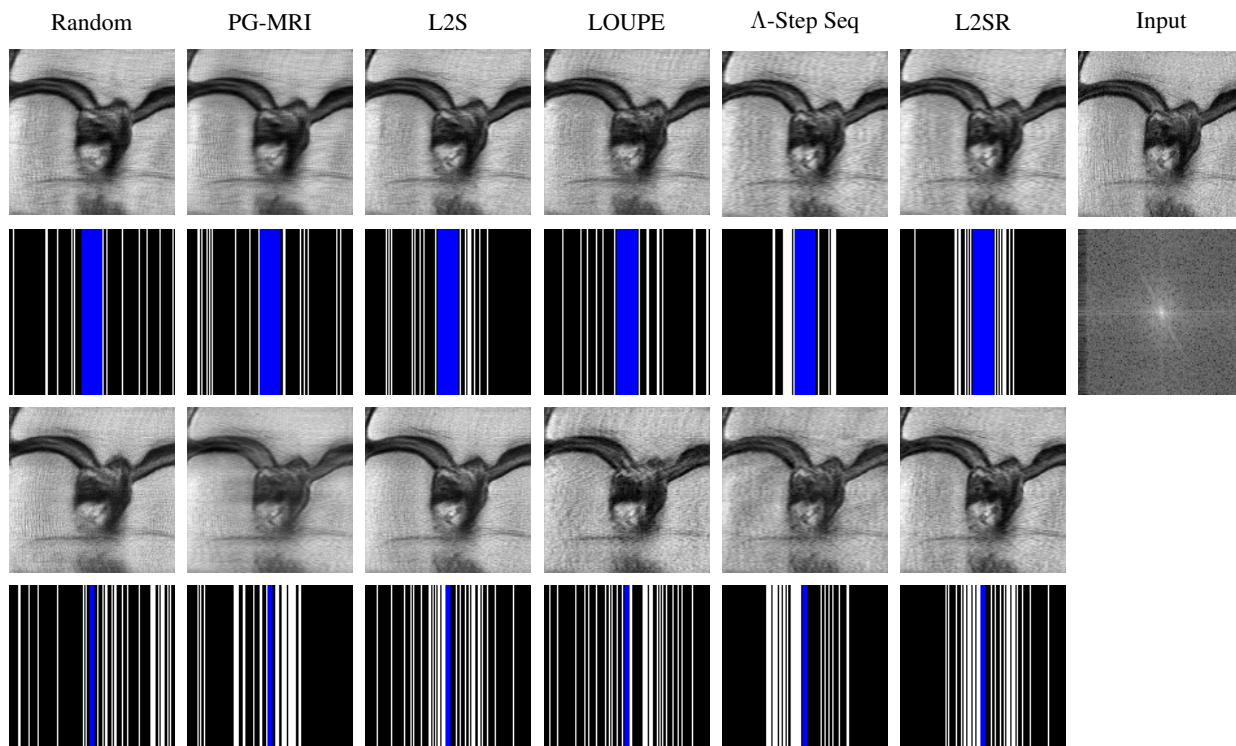


Figure 8. Visualisation of an example of the knee dataset for our methods and other competing methods under  $\times 4$ -acceleration.

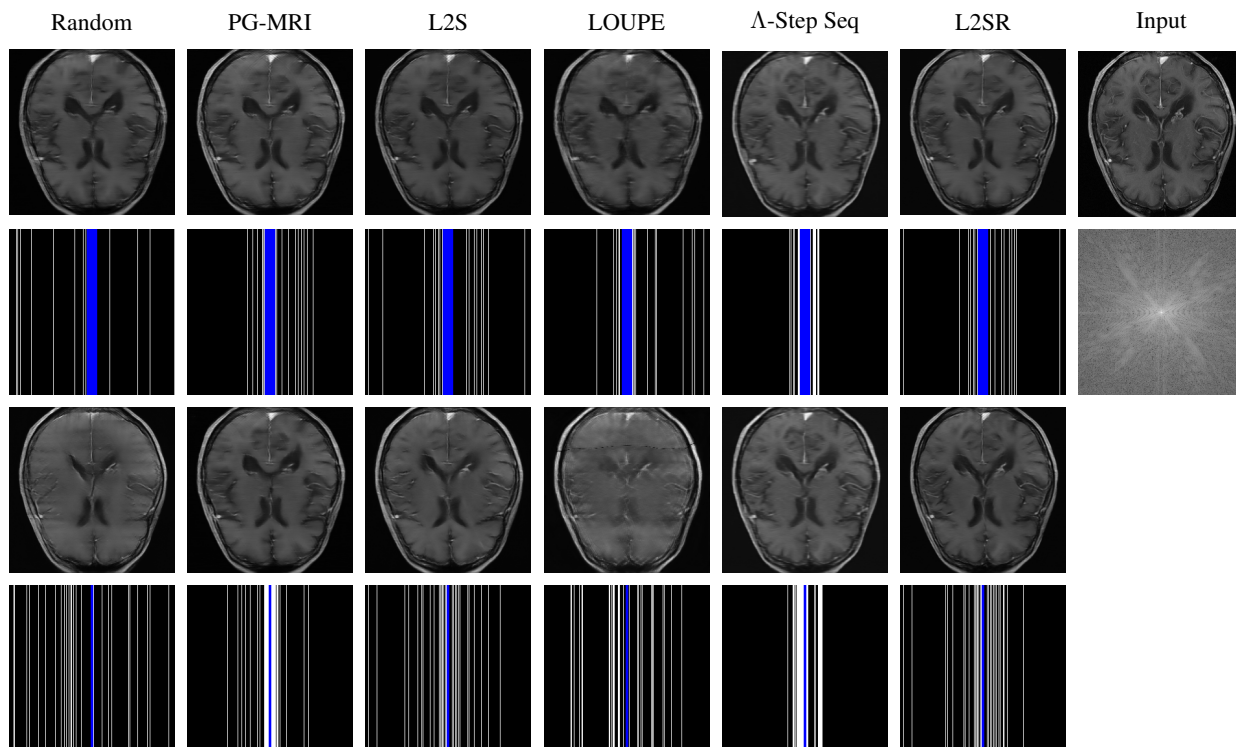


Figure 9. Visualisation of an example of the brain dataset for our methods and other competing methods under  $\times 8$ -acceleration.

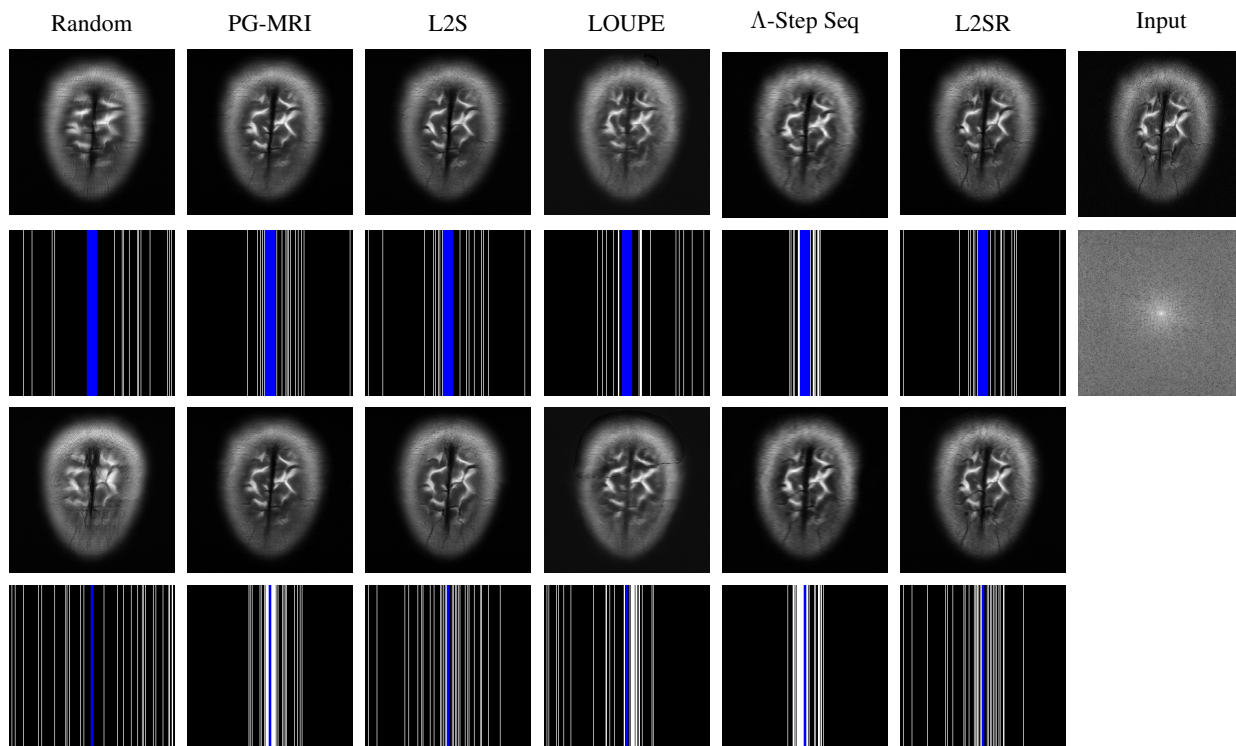


Figure 10. Visualisation of an example of the brain dataset for our methods and other competing methods under  $\times 8$ -acceleration.